Earth Planet. Sci. Lett. 658 (2025) 119306

Contents lists available at ScienceDirect

Earth and Planetary Science Letters

journal homepage: www.elsevier.com/locate/epsl

Eccentricity and obliquity forcing of East Asian hydroclimate during the latest Cretaceous to early Paleocene

Xiaoyue Zhang [a], David B. Kemp [a,*], Ruiyao Zhang [b], Robert A. Spicer [c,d,e], Simin Jin [f], Rui Zhang [b], Ze Zhang [f], Chunju Huang [a,*]

[a] *State Key Laboratory of Geomicrobiology and Environmental Changes, Hubei Key Laboratory of Critical Zone Evolution, School of Earth Sciences, China University of Geosciences, Wuhan 430074, China*
[b] *College of Urban and Environmental Sciences, Hubei Normal University, Huangshi 435002, China*
[c] *CAS Key Laboratory of Tropical Forest Ecology, Xishuangbanna Tropical Botanical Garden, Chinese Academy of Sciences, Mengla 666303, China*
[d] *School of Environment, Earth and Ecosystem Sciences, The Open University, Milton Keynes MK7 6AA, UK*
[e] *State Key Laboratory of Tibetan Plateau Earth System, Environment and Resources, Institute of Tibetan Plateau Research, Chinese Academy of Sciences, Beijing 100101, China*
[f] *Department of Atmospheric Science, School of Environmental Studies, China University of Geosciences, Wuhan 430074, China*

ARTICLE INFO

Edited by: Dr H. Bao.

Keywords:
Cyclostratigraphy
Hydroclimate
Latest Cretaceous
Early Paleocene
Gonjo Basin

ABSTRACT

The latest Cretaceous to early Paleocene was characterized by a global 'greenhouse' climate, and may provide a useful analogue for understanding hydroclimate responses to elevated atmospheric CO_2 and temperature. However, a paucity of high-resolution and temporally well-constrained continental sedimentary records spanning this time interval hinders our understanding. We address this issue via a high-resolution paleoenvironmental analysis of a ∼1305 m thick terrestrial succession from the Asian interior (Gonjo Basin, Southeast Tibet). Cyclostratigraphic analysis of element abundance data, combined with a published magnetostratigraphy, allows us to establish an astronomical timescale spanning the latest Cretaceous to early Paleocene (∼69.4 Ma to ∼58.5 Ma) and investigate climatic variations at an orbital time-scale. We show that the paleoenvironment of the Gonjo Basin underwent two key transitions, with a shift from braided river conditions to floodplain-dominated conditions at ∼68.8 Ma, followed by a return to braided river conditions with likely high seasonality at ∼63.5 Ma. Eccentricity and obliquity forcing exerted a strong control on the regional hydrological cycle. We show that the relative strength of obliquity was likely amplified compared to coeval marine records. Obliquity may have modulated meridional heat and moisture transport into the Asian interior, which, combined with feedbacks from quasi-stable carbon reservoirs, mediated hydroclimate. This study improves our understanding of continental paleoclimate evolution in the latest Cretaceous to early Paleocene, and establishes the role and mechanisms of orbital forcing as a driver of hydrological cycle change in East Asia at this time.

1. Introduction

Increasing atmospheric pCO_2 concentrations and global warming at the present day are expected to lead to changing precipitation patterns and the increased occurrence of climate extremes, especially droughts and floods, together affecting water and food security globally (IPCC, 2023). The latest Cretaceous to early Paleocene, characterized by a broadly sustained global greenhouse climate, may be a useful time interval for better understanding how hydroclimate operates during increased global warmth. Benthic foraminifera oxygen isotope data ($\delta^{18}O_b$) indicate an overall warming trend from the late Maastrichtian to Paleocene, with the coolest conditions occurring in the middle Paleocene (∼61 Ma to ∼58 Ma), and the warmest conditions occurring at the Paleocene-Eocene boundary (∼56 Ma) and in the early Eocene (Zachos et al., 2001; Barnet et al., 2019). Superimposed on the overall greenhouse climate and long-term trends were transient climatic perturbations (e.g., Barnet et al., 2019).

Compared to marine records, temporally well-constrained terrestrial records across the latest Cretaceous to early Paleocene are rare – especially long, continuous, and high-resolution records. This hinders our understanding on how continental interiors respond to relative global warmth. Sediment facies and paleobotanical research suggest that a

* Corresponding authors.
E-mail addresses: davidkemp@cug.edu.cn (D.B. Kemp), huangcj@cug.edu.cn (C. Huang).

https://doi.org/10.1016/j.epsl.2025.119306
Received 22 October 2024; Received in revised form 2 February 2025; Accepted 6 March 2025
Available online 13 March 2025

broad arid belt existed across much of China in the latest Cretaceous to Paleocene (Sun and Wang, 2005; Ma et al., 2021; Zhang et al., 2024a). Magnetic susceptibility and geochemical data from 72 Ma to 62.8 Ma in the low latitude Nanxiong Basin (Southeast China) demonstrate broad trends that are consistent with global climatic evolution inferred from marine records. Magnetic susceptibility and bulk carbonate carbon isotope data from a shorter interval in the Nanxiong Basin (~66.6–65 Ma) show eccentricity cycles (Ma et al., 2022), although the age model for the basin remains controversial (Ma et al., 2018). Multiproxy data (e.g., illite chemistry index, chemical index of alteration (CIA), and stable and clumped isotopes of pedogenic carbonate and clay minerals) from the mid-latitude terrestrial Songliao Basin (Northeast China) spanning the latest Cretaceous to earliest Paleogene reveal that the hydroclimate in this basin responded sensitively to global temperature fluctuations

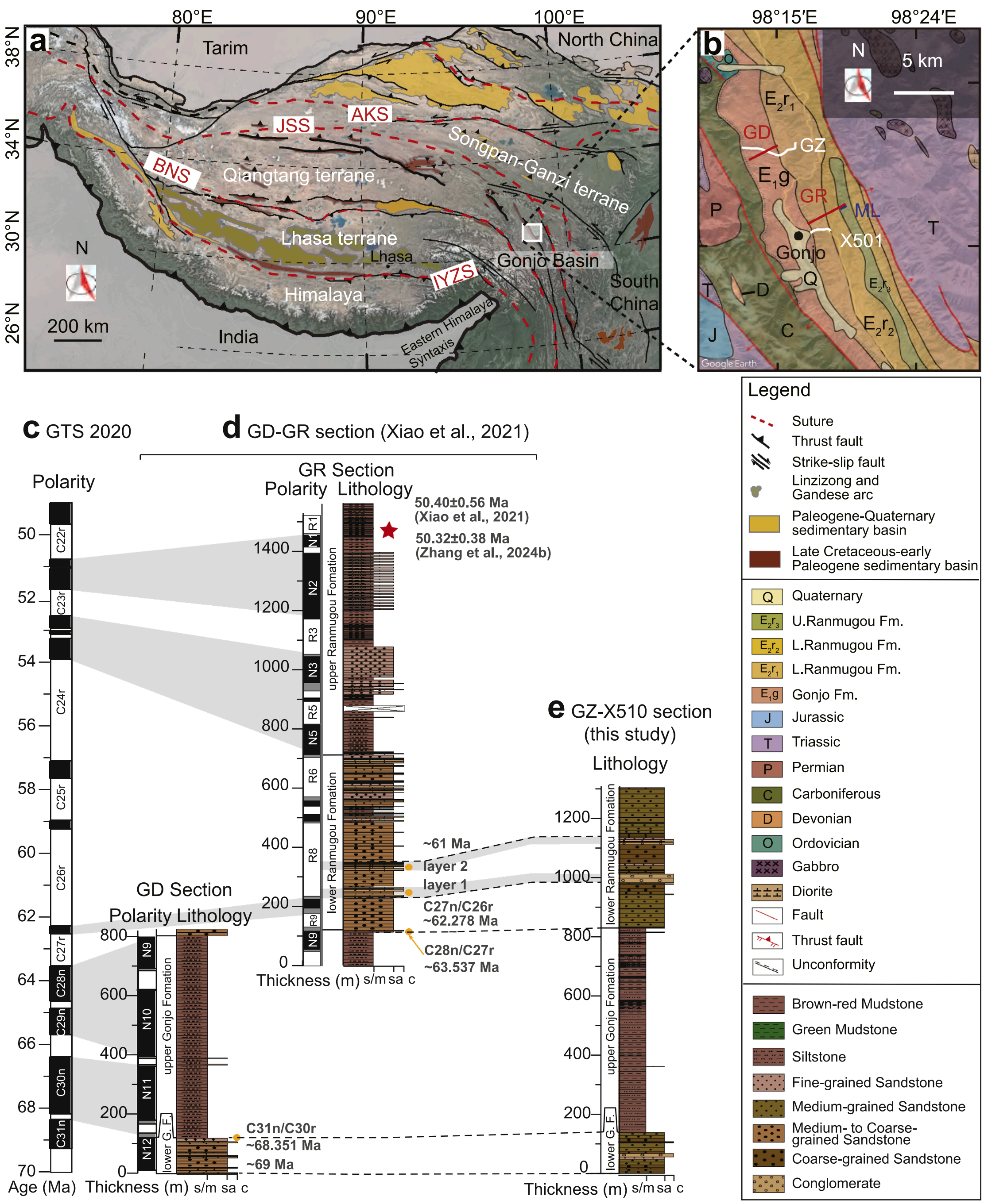

Fig. 1. Geological maps and stratigraphic details of the studied Gonjo Basin strata. (a) Simplified topographic map and tectonic framework of the Tibetan Plateau and adjacent regions, modified from Spurlin et al. (2005). The pale square shows the location of the studied Gonjo Basin, enlarged in (b). (b) Geological map of the Gonjo Basin (modified from BGMR Xizang, 1993). The white lines show the sampled Gonzhong (GZ) and X501 sections. The red lines show the Gongzhong-Dongtuo (GD) and Gonjo-Ranmugou (GR) sections (Xiao et al., 2021), and the blue line shows the Milai (ML) section (Zhang et al., 2024b). (c) Geologic Time Scale (GTS2020; Gradstein et al., 2020). (d) Lithostratigraphy and magnetostratigraphy of the GD-GR composite section from Xiao et al. (2021). Red star marks the stratigraphic position of the volcaniclastic layer analyzed in Xiao et al. (2021). An altered Andesite zircon U-Pb date (within error of Xiao et al.'s date) likely corresponds to the same horizon analyzed by Xiao et al. (2021) (Zhang et al., 2024b). Gray magnetozones highlight sampling gaps in the magnetostratigraphy. (e) Lithology of the studied GZ-X501 section. Lithostratigraphic correlation between GD-GR and GZ-X501 sections is based on 4 key horizons (orange circles), see Supplementary Material Text 1 for details.

(Gao et al., 2021). At orbital scales, high-resolution thorium (Th) logging data, gamma-ray (GR) and magnetic susceptibility (MS) data from the Songliao Basin suggest wet/dry runoff cycles in the basin were mediated by orbital forcing (i.e. eccentricity, obliquity and precession) in the latest Cretaceous to earliest Paleocene (Wu et al., 2009, 2013, 2014; Wang et al., 2013). Despite these existing studies, a wider geographical coverage of high resolution and relatively long-duration hydroclimate records is still needed to more fully elucidate the pattern and drivers of latest Cretaceous to early Paleocene terrestrial climate variability in the Asian interior.

To further understand hydroclimate changes and forcing mechanisms during the latest Cretaceous to early Paleocene, we studied a thick (~1305 m) terrestrial sedimentary record from the Gonjo Basin (southeast Tibet). We present new sedimentological and high-resolution XRF element abundance data from this record, and combine it with cyclostratigraphic analysis and a published magnetostratigraphy to establish a high-resolution record of paleoenvironmental change and an astronomical timescale. Based on this, we assess the paleoenvironmental evolution of the basin in the context of the global warmth of the latest Cretaceous to early Paleocene, and infer the role and mechanisms of orbital forcing as a driver of hydrological cycle change in East Asia at this time.

2. Geological setting

The Gonjo Basin is located in the southeastern part of the Tibetan Plateau region. It is a narrow NNW-SSE orientated basin located towards the eastern end of the Qiangtang Terrane (Fig. 1a). The basin is characterized by reverse faults and a basin-scale asymmetrical syncline. The Gonjo Basin developed on Ordovician, Carboniferous and Triassic basement (Fig. 1b) (Xiao et al., 2021). The basin exposes continental red bed strata with relatively minor tectonic deformation (Studnicki-Gizbert et al., 2008; Xiao et al., 2021). The sedimentary strata of the central Gonjo Basin consist of the Gonjo Formation conformably overlain by the Ranmugou Formation. Each formation is further divided into lower and upper units (Xiao et al., 2021). The facies of the Gonjo and lower Ranmugou formations comprise mainly red clastic lithologies, with occasional paleosols. The sedimentary environments for these deposits varied between braided river, distal alluvial fan and floodplain (Xiong et al., 2020; Xiao et al., 2021). Rocks in the upper Ranmugou Formation are characterized by reddish-brown and greenish fine-grained sandstone, siltstone, mudstone, and occasional gypsum layers deposited in a mainly lacustrine environment (Xiao et al., 2021).

Paleobotanical research (e.g., sporopollens and leaves including palm fossils) suggests that the age of the Gonjo red beds ranges from Paleocene to Oligocene (e.g., He et al., 1983; BGMR Xizang, 1993; Studnicki-Gizbert et al., 2008). $^{40}Ar/^{39}Ar$ and U-Pb dating conducted on volcanic rocks from the uppermost strata (i.e. upper Ranmugou Formation) constrained the minimum depositional age of sediments in the northern and southern Gonjo Basin to ~43–44 Ma (Studnicki-Gizbert et al., 2008; Tang et al., 2017; Xiong et al., 2020), and in the central basin to ~50.4–50.3 Ma (Xiao et al., 2021; Zhang et al., 2024b). Recent magnetostratigraphic work, tied to radiometric dates, indicates a ~69–41.5 Ma age (Li et al., 2020a) or ~69–50 Ma age (Xiao et al., 2021) for the strata in the central basin. In detail, Xiao et al. (2021) used volcaniclastic zircon U-Pb dating from the upper part of their section to anchor the magnetostratigraphy in numerical time, with this dating supported by recent U-Pb dating of zircons in altered Andesite from the central basin (Zhang et al., 2024b) (Fig. 1c-d). By contrast, Li et al. (2020a) used volcanic rock ages from the northern basin to anchor their magnetostratigraphy.

3. Materials and methods

3.1. Logging and sampling

Two stratigraphic sections were measured in the central Gonjo Basin: the Gongzhong (hereafter GZ) section (30.94° N, 98.26°E) near Gongzhong village, and the X501 section (30.87° N, 98.29°E) along the X501 road (Fig. 1b). The two sections are correlated using lithostratigraphy to generate a composite section (GZ-X501 section) (Fig. 1e). The GZ-X501 section covers the whole Gonjo Formation and part of the lower Ranmugou Formation (Fig. 1b). Our GZ-X501 section is readily correlated lithostratigraphically to the GD-GR composite section of Xiao et al. (2021), also measured in the central basin close to our section (Fig. 1b and d) (see Supplementary Material Text 1). A total of ~5100 rock samples were collected along the ~1305 m thick GZ-X501 section at sampling intervals of 5–75 cm.

The GZ-X501 section was logged at high-resolution (see Supplementary Material Text 1 for a full description of the lithostratigraphy), with lithologies numerically categorized (ranked) according to grain size using the following scheme to create a time series of "lithorank" values: 1 = mudstone, 2 = siltstone, 3 = fine-grained sandstone, 4 = medium-grained sandstone, 5 = coarse-grained sandstone, 6 = conglomerate (Fig. 2a).

3.2. Geochemical data

The abundance of Al, Si, K, Ca, Ti, Fe, Mn, Rb, Sr and Zr were measured with a handheld Innov-X Systems X-ray fluorescence (XRF) spectrometer in geochemistry mode operated at 50 kv (beam 1), and 10 kv (beam 2). All samples were cut on a rotating abrasive disc (skimmer) prior to analysis to get a flat surface suitable for measurement. Each sample was tested three times, each time for 60 s, and the average element abundance values were calculated. The precision of the obtained data (based on repeat measurement of samples) was ~2.37 %, ~0.53 %, ~0.81 %, ~0.45 %, ~5.72 %, ~5.23 %, ~0.59 %, ~2.13 %, ~1.63 % and ~1.65 % for Al, Si, K, Ca, Ti, Mn, Fe, Rb, Sr and Zr, respectively (relative standard deviations).

3.3. Principal component analysis

Principal Component Analysis (PCA) is a multivariate analysis method for reducing the dimensionality of data without losing important information (Jolliffe and Cadima, 2016). PCA was performed on the raw XRF data using the built-in R functions "prcomp", and we extracted and visualized the results using the R package "factoextra" (https://cloud.r-project.org/package=factoextra/) (for the code see Supplementary Material Text 2). The calculation is computed using singular value decomposition of the centered and standardized data matrix and generates a set of variables called principal components (PC) by projecting the original data points onto the major eigenvector(s) representing most of the data variance (Jolliffe and Cadima, 2016; Lanci et al., 2022). The standardization is to make the variables comparable, and the data are normalized to have a standard deviation of one and zero mean. Eigenvalues (i.e. the amount of variance retained by each principal component) and the correlations between variables and PCs were also computed. The XRF data matrix (Al, Si, K, Ca, Ti, Fe, Mn, Rb, Sr and Zr) was analyzed using PCA, and the first principal component (PC1, which accounts for the highest proportion of variance in the data) is used for cyclostratigraphic analysis to establish an astronomical timescale (ATS) for the GZ-X501 section. To complement this approach, we also utilized K/Rb ratio data for paleoenvironmental interpretation and cyclostratigraphic analysis. K/Rb data can be a potential indicator of weathering intensity (see Supplementary Material Text 3).

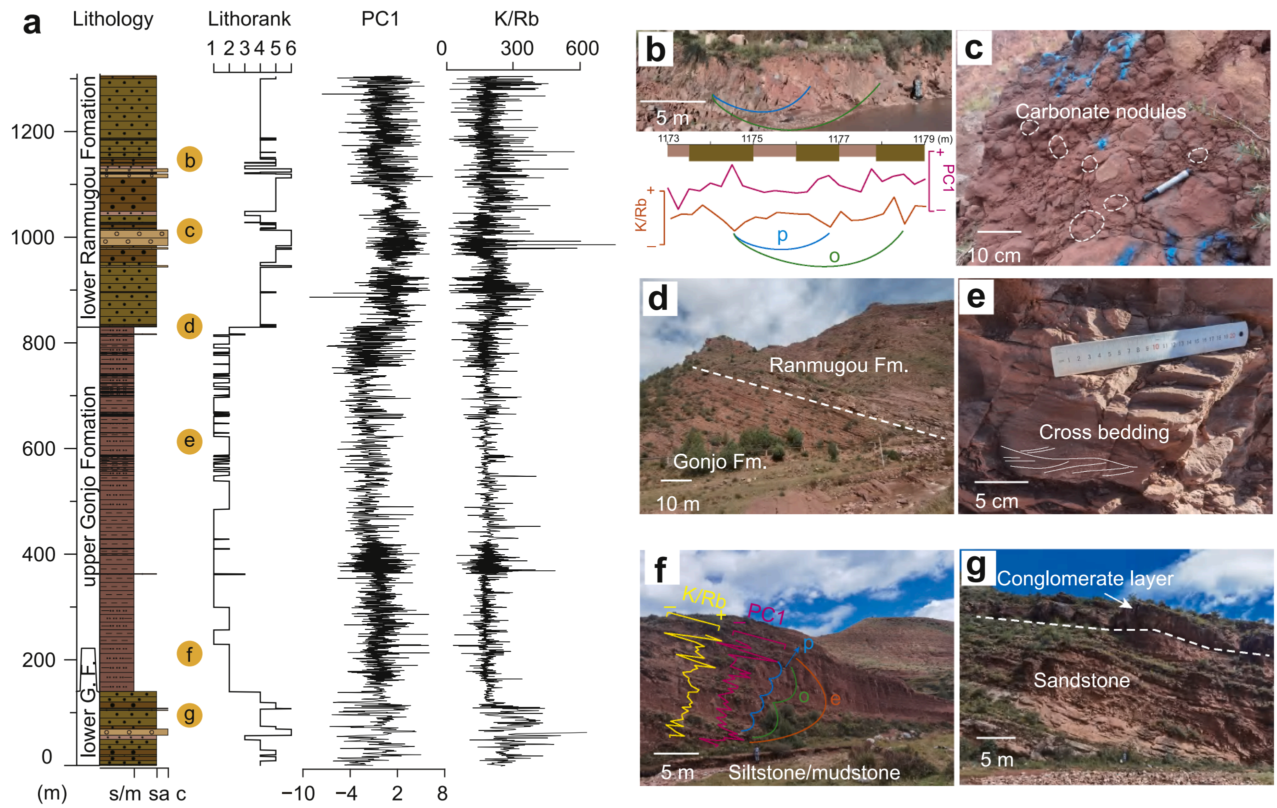

Fig. 2. Lithostratigraphy, paleoenvironmental proxies and representative field photographs of the studied GZ-X501 section in the Gonjo Basin. (a) Lithology and paleoenvironmental proxies of the measured GZ-X501 section. Lithorank values are explained in Section 3.1. PC1 and K/Rb data are also shown. Orange circles mark the position of field photographs (b)-(g) shown on right. (b) Dominantly fine- to medium- grained sandstone of braided river environment (~1173–1179 m section height, lower Ranmugou Formation). Lithology, PC1 and K/Rb variations and cyclostratigraphic interpretation also shown. (c) Carbonate nodules in the lower Ranmugou Formation (~1114 m section height). (d) Conformable contact between the Gonjo Formation and lower Ranmugou Formation (~830 m section height). (e) The siltstone in the upper Gonjo Formation with climbing ripple cross-bedding (~614 m section height). (f) Dominantly brown-red siltstone and mudstone of floodplain environment (~205–215 m section height, upper Gonjo Formation). The orange, green and blue lines highlight the inferred short-eccentricity, obliquity and precession cycles, respectively. (g) Medium-grained sandstone interbedded with fine-grained sandstones of the lower Gonjo Formation (~90–107.5 m section height). At the top is a conglomerate layer (~1 m thick) with an erosive base (~107.5 m section height).

3.4. Time series analysis

After removing conglomerate layers that were likely deposited geologically instantaneously, 2π multitaper method (MTM) spectral analysis (Thomson, 1982) was carried out on linearly interpolated, demeaned and detrended PC1 and K/Rb data. Robust red noise modeling (Mann and Lees, 1996) was used to identify any anomalously high narrow-band variance that could be related to astronomical cycles. To augment this approach, the method of smoothed window averaging (SWA) and false discovery rate (FDR) significance testing (Weedon et al., 2019) was used to test the significance of inferred cycles in our ATS. The correlation coefficient (COCO) and evolutionary correlation coefficient (eCOCO) analysis methods (Li et al., 2018) were used to indicate likely sedimentation rates. Following astronomical cycle interpretation, data were tuned by fixing the duration of identified cycles to the inferred astronomical period, facilitated by Gaussian bandpass (Kodama and Hinnov, 2014). Power decomposition analysis (Li et al., 2016) was used to track the strength of inferred astronomical cycles through time in the tuned data. All time series analyses were conducted using Acycle v2.8 software (Li et al., 2019b, see Supplementary Material Text 4 for additional details).

4. Results

4.1. Lithostratigraphy and geochemical trends

The broad lithological variability of the GZ-X501 section is reflected in the obtained geochemical data (Fig. 2). The first principal component (PC1) of the XRF data captures the dominant element composition variability in the GZ-X501 section, and shows clear correlation with lithology, the lithorank values, and element abundance variations related to grain size (Figs. 2 and 3; Tables S1 and S2; see also Supplementary Material Text 3). Where well-exposed at outcrop, intervals of strata dominated by either floodplain or braided river deposits show lithological variations that can be linked to changing geochemistry, with high PC1 and low K/Rb values corresponding to relatively coarser grained sandstone layers, and low PC1 and high K/Rb values corresponding to relatively finer grained sandstone and mudstone layers (Fig. 2b and f).

4.2. Cyclostratigraphy

4.2.1. Spectral analysis, COCO and eCOCO results

To prepare PC1 and K/Rb data for cyclostratigraphic analysis, 6 conglomerate beds (at 57.75–69 m, 943.5–946.25 m, 977.48–980.04 m, 984.12–1013.25 m, 1112.5–1119.5, 1123.5–1129.5 m), that represent inferred alluvial fan/flood event beds, were removed (Fig. S3). This yields a 1244.25 m succession (4817 datapoints; Fig. 4a). The evolutionary wavelet power spectrum of the PC1 data shows evidence for ~2.5 m, ~7 m and ~20 m cycles through ~0–130 m; ~3 m, ~9–11 m, ~23 m and ~81 m cycles through ~130–400 m; ~3 m, ~13 m, ~36 m and ~160 m cycles through ~400–700 m; and ~6.7 m, ~10–12.5 m, ~27–40 m, ~66 m and ~160 m cycles through ~700–1244.25 m (Fig. 4b). The eCOCO analysis suggests that sedimentation rates were

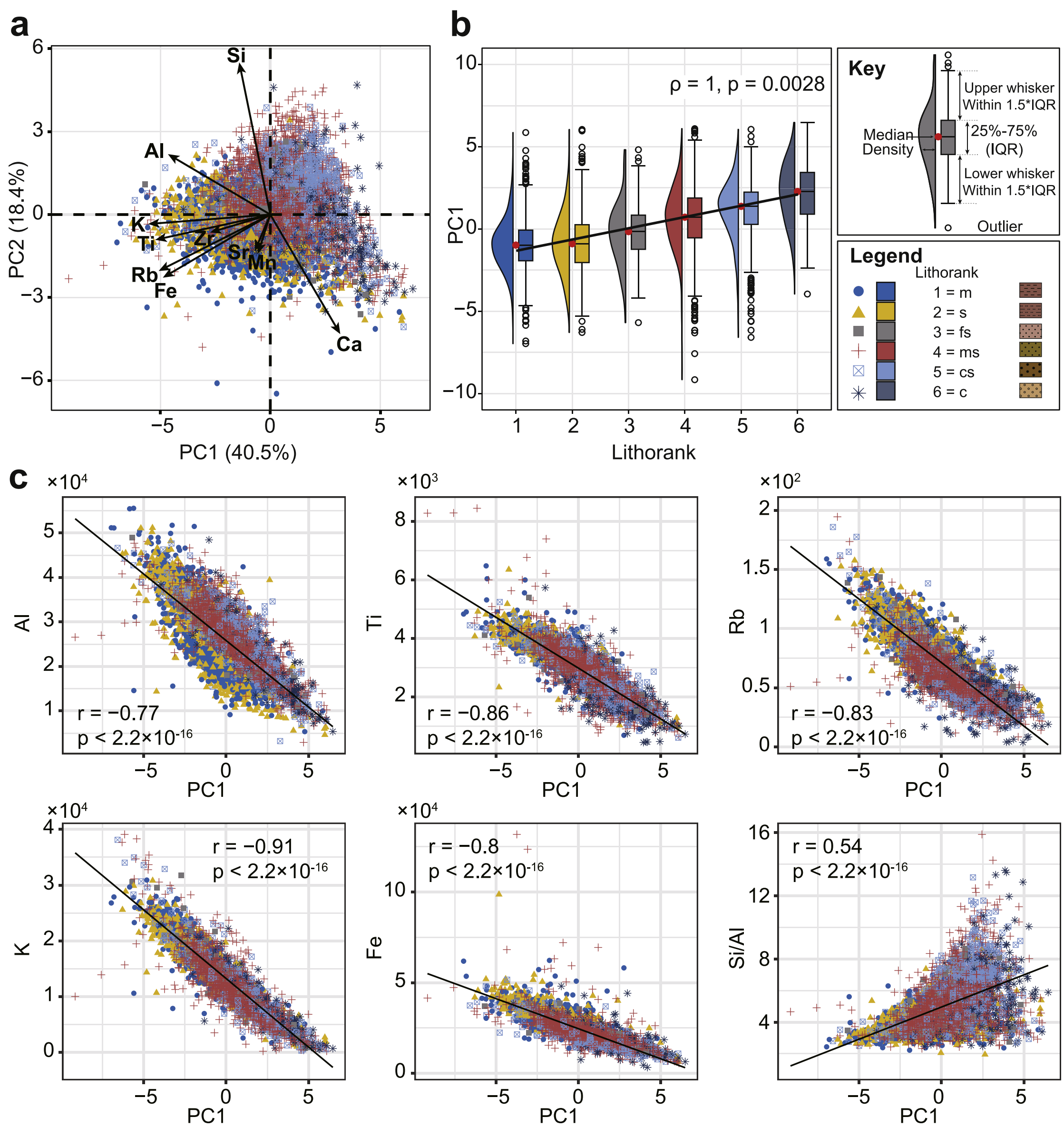

Fig. 3. PCA results of the XRF data and correlations between PC1 and other paleoenvironmental proxies. (a) PCA results, visualized using a simple biplot of individual data and variables of XRF data (black arrows). Different colored scatter points are used to distinguish different lithological groups based on lithorank values (Section 3.1). The relationship between lithology and the first two principal components (PC1 and PC2) is also shown. The direction of the black arrow shows the correlation between the variable in XRF data (Al, Si, K, Ca, Ti, Fe, Mn, Rb, Sr, Zr; Fig. S1) and the principal component (PC1 and PC2; Fig. S2). The relative length of the arrows represents the degree of correlation – the longer the length the higher the Pearson correlation coefficients. (b) Relationship between PC1 values and facies. Box-violin plots of the distribution of PC1 values within the 6 lithological (lithorank) groups. The black solid line shows the linear correlation between the lithorank value and median PC1 (Spearman ρ=1; p-value=0.0028). (c) Scatter plots with Pearson correlation coefficients and p-values showing the relationships between PC1 values and various XRF data.

~8 cm/kyr or ~19 cm/kyr at ~0–200 m, ~12 cm/kyr or ~29 cm/kyr at ~200–410 m, ~33 cm/kyr at ~410–700 m, and ~9 cm/kyr or ~30–40 cm/kyr at ~700–1244.25 m (Fig. 4c). The paleomagnetic timescale inferred by Xiao et al. (2021) for the nearby GD-GR section suggests that sedimentation rates varied from 3.7 cm/kyr to 31.3 cm/kyr through their studied interval, broadly consistent with our results (Fig. 4c).

The length of the studied succession, and the variety of facies preserved, indicates that the sedimentation rate of the succession was likely to have varied – a deduction supported by our wavelet and eCOCO analyses (Fig. 4b-c). Based on the wavelet analysis results and the lithostratigraphy, PC1 data were divided into six parts for subsequent time-series analysis: Part 1 (0–128 m), Part 2 (128–410 m), Part 3 (410–700 m), Part 4 (700–818 m), Part 5 (818–1050 m) and Part 6 (1050–1244.25 m) (Figs. 4a-c and S3). MTM analysis of the PC1 data in these separate parts shows statistically significant (>95 % confidence level) peaks at ~20 m, ~8–6 m, and ~2.7 m in Part 1 (Fig. 5f), peaks at ~11.1 m, ~6.8 m, ~4.8 m and ~3 m in Part 2 (Fig. 5e), peaks at ~35 m, ~12.7 m, ~7.9 m, ~3.8 m and ~2.5 m in Part 3 (Fig. 5d), peaks at ~12 m, ~6.7 m, ~3.4 m, ~2.7 m and ~1.6 m in Part 4 (Fig. 5c), peaks at ~40 m, ~10 m, ~3.85 m and ~1.9 m in Part 5 (Fig. 5b), and peaks at ~33 m, ~9 m, ~3 m, and ~2.2 m in Part 6 (Fig. 5a). As a complementary approach, K/Rb data were also segmented and analyzed in the same way as the PC1 data. The MTM results for the K/Rb data are similar to PC1 data (Supplementary Material Text 5; Fig. S5).

4.2.2. Astronomical tuning

Based on the COCO results, the sedimentation rate of Part 1 was 6.2 cm/kyr, 8.1 cm/kyr or ~19.9 cm/kyr (Figs. 4d and S4). The higher

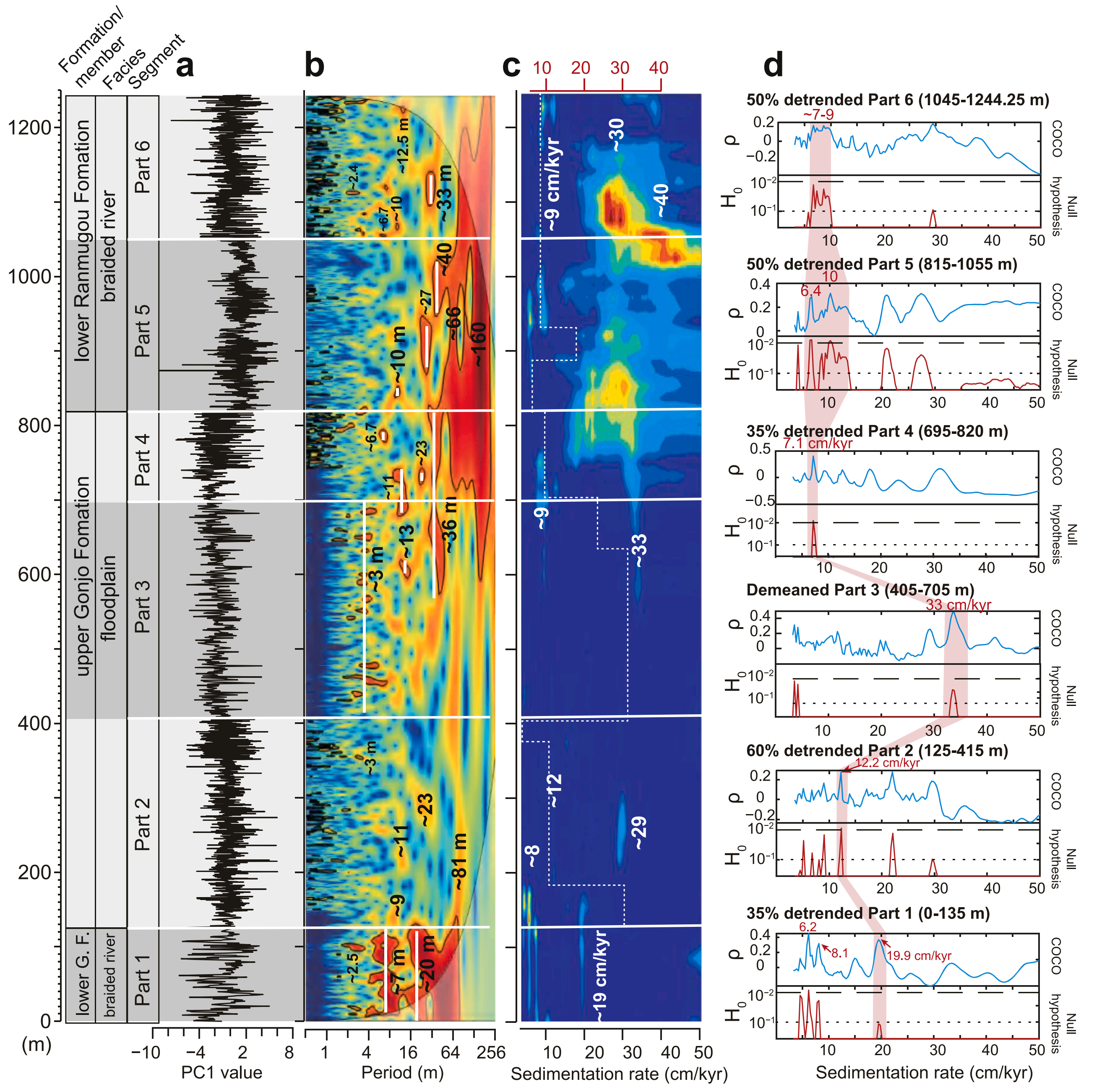

Fig. 4. Wavelet analysis, COCO and eCOCO results of the PC1 data of the GZ-X501 section. (a) PC1 data, showing subdivision into 6 parts. (b) Wavelet spectrogram of PC1 data after 35 % rLOESS detrending. (c) eCOCO results of the PC1 data after 35 % rLOESS detrending. Tested sedimentation rates ranged from 3.25 to 50 cm/kyr, with a step of 0.3225 cm/kyr. The number of Monte Carlo simulations used was 10,000. The sliding window size in the eCOCO analysis was 175 m, with a step of 4.25 m. Astronomical solution used is La2004 (Laskar et al., 2004). See Supplementary Material Text 4 and Li et al. (2018) for further details. White dotted lines highlight the sedimentation rate estimates derived from magnetostratigraphy of Xiao et al. (2021). (d) COCO results of segmented PC1 data after rLOESS detrending or demeaning. Tested sedimentation rates ranged from 3.25 to 50 cm/kyr, with a step of 0.3225 cm/kyr. The number of Monte Carlo simulations used was 10,000. Astronomical solution is La2004 (Laskar et al., 2004). Red shading in f highlights the likely optimal sedimentation rate estimated by COCO. Because Parts 1, 3 and 4 are short, which may compromise the ability to identify long duration cycles related to 405 kyr long eccentricity cycles, the analysis of these parts was performed using La2004 as the astronomical solution, but excluding the 405 kyr cycle, and the significance (inferred by H_0) of the optimal sedimentation rate was consequently enhanced (Fig. S4).

sedimentation rate (~19.9 cm/kyr) is most likely given the coarseness of the sediment in this part compared to strata above. A lower sedimentation rate (~6–8 cm/kyr) would also imply that the strong ~20 m cycles in this part have durations of ~286 kyr, which is inconsistent with any orbital cycle. Based on this, the ~20 m and ~8–6 m peaks observed in the MTM spectrum for Part 1 are inferred to be ~100 kyr short-eccentricity and ~40 kyr obliquity, respectively (Fig. 5f).

In Part 2, the COCO plot shows the most significant peak at ~12.2 cm/kyr (H_0 < 0.01) (another peak at ~22 cm/kyr has H_0 > 0.01, Fig. 4d). This part is characterized by a floodplain environment with finer grained sediment, which might suggest a lower sedimentation rate relative to Part 1. Taken together, the sedimentation rate at ~12.2 cm/kyr is the optimal sedimentation rate, implying that the ~11.1 m, ~4.8 m and ~3 m spectral peaks in Part 2 represent ~100 kyr short-eccentricity cycles, ~40 kyr obliquity cycles and ~20 kyr precession cycles, respectively (Fig. 5e). In this part in particular, these cycles are

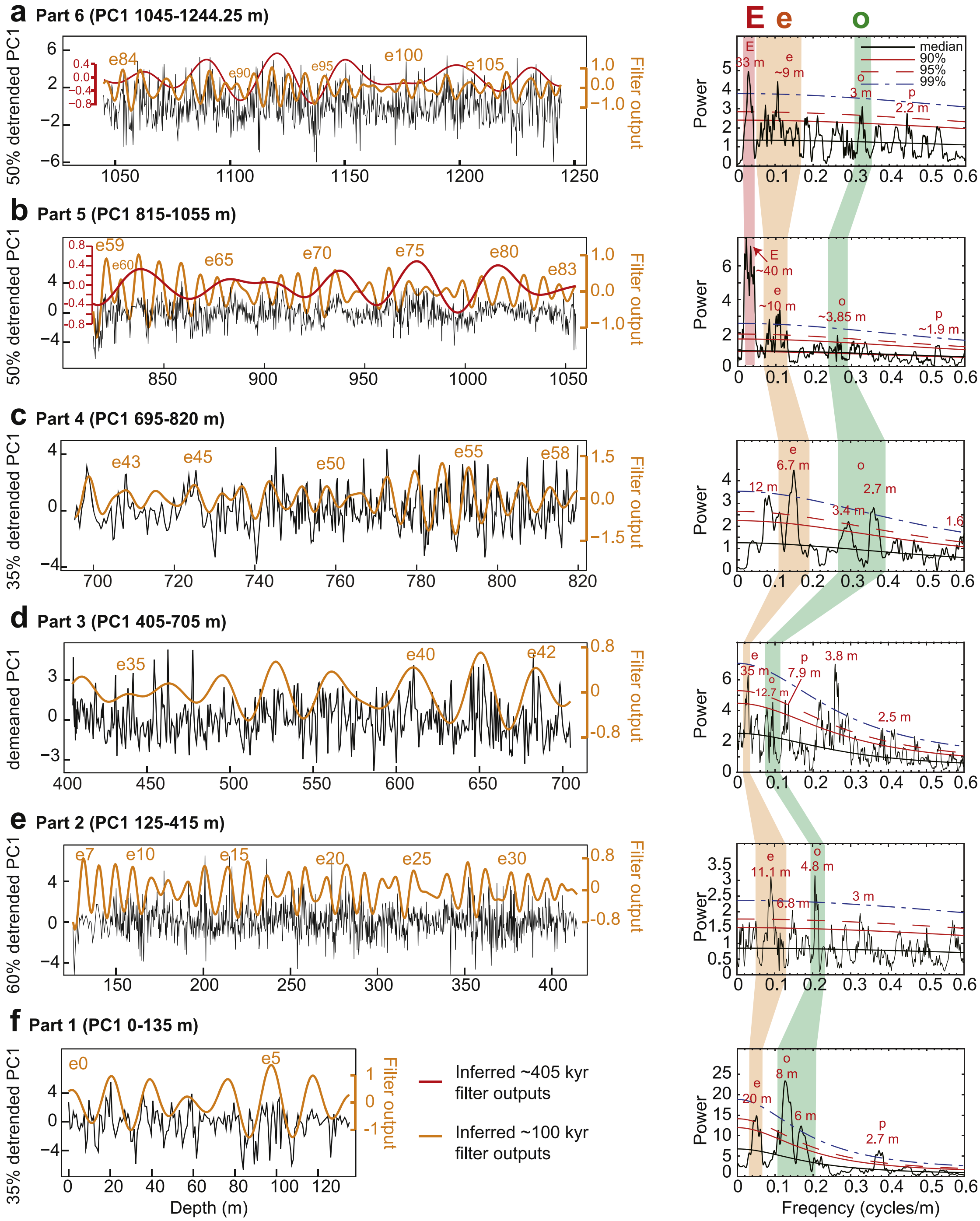

Fig. 5. PC1 data of the GZ-X501 section shown with interpreted long-eccentricity (405 kyr, red lines) and short-eccentricity (~100 kyr, orange lines) cycles for each part, and the associated 2π MTM power spectra. (a) PC1 data in Part 6 shown with ~33 m and ~9 m filtered cycles (bandpass filters set at 0.03 ± 0.015 cycles/m and 0.11 ± 0.06 cycles/m, respectively) (left) and corresponding 2π MTM power spectrum (right). (b) PC1 data in Part 5 shown with ~40 m and ~10 m filtered cycles (bandpass filters set at 0.025 ± 0.01 cycles/m and 0.1 ± 0.03 cycles/m, respectively) (left) and corresponding 2π MTM power spectrum (right). (c) PC1 data in Part 4 show with ~6.7 m filtered cycles (bandpass filter set at 0.1493 ± 0.0377 cycles/m) (left) and corresponding 2π MTM power spectrum (right). (d) PC1 data in Part 3 show with ~35 m filtered cycles (bandpass filter set at 0.0286 ± 0.009 cycles/m) (left) and corresponding 2π MTM power spectrum (right). (e) PC1 data in Part 2 show with ~11 m filtered cycles (bandpass filter set at 0.09 ± 0.0375 cycles/m) (left) and corresponding 2π MTM power spectrum (right). (f) PC1 data in Part 1 shown with ~20 m filtered cycles (bandpass filter set at 0.05 ± 0.15 cycles/m) (left) and corresponding 2π MTM power spectrum (right). Red, orange and green shading represents long-eccentricity, short-eccentricity and obliquity, respectively.

observable at outcrop thanks to the good exposure (Fig. 2f).

In Parts 3 and 4, the COCO plots show significant peaks at ~33 cm/kyr and at ~7.1 cm/kyr, respectively (Fig. 4d and S4). Thus, the ~35 m, ~12.7 m and ~7.9 m peaks in Part 3 likely represent ~100 kyr short eccentricity, ~40 kyr obliquity and ~20 kyr precession cycles (Fig. 5d), and the ~6.7 m, ~3.4–2.7 m and ~1.6 m peaks in Part 4 likely also represent ~100 kyr, ~40 kyr and ~20 kyr cycles, respectively (Fig. 5c). The ~12 m peak in Part 4 may represent ~173 kyr obliquity amplitude modulation (AM) cycles (Fig. 5c). The ~3.8 m and ~2.5 m peaks in Part 3 (Fig. 5d) might be related to suborbital cycles or be caused by a low sampling resolution (~0.75 m) in this interval. The inferred sedimentation rate change between Parts 2 and 4 (from 128 m to 818 m) is similar to the sedimentation rate pattern inferred by Xiao et al. (2021) (who inferred a change from <11 cm/kyr to ~20–30 cm/kyr, and back to 9.6 cm/kyr; Fig. 6). Part 3 has a higher sedimentation rate compared with the other parts according to the COCO analysis (Fig. 4d). The strata are homogeneous in this part, with limited lithological changes. Cross bedding and parallel bedding are developed in siltstone lithologies in Part 3 (Fig. 2e), suggesting an enhanced hydrodynamic regime and perhaps relatively high sediment supply, consistent with the inference of higher sedimentation rate.

In Parts 5 and 6, the COCO results suggest sedimentation rates of ~6.4 cm/kyr or ~10 cm/kyr in Part 5, and ~7 cm/kyr or ~9 cm/kyr in Part 6 (Fig. 4d). MTM peaks at ~40 m, ~10 m, ~3.85 m and ~1.9 m in Part 5 can thus be assigned to ~405 kyr long-eccentricity, ~100 kyr short-eccentricity, ~40 kyr obliquity, and ~20 kyr precession, respectively (Fig. 5b). The inferred mean sedimentation rate in Part 5 was ~10 cm/kyr. Similarly, the MTM peaks at ~33 m, ~9 m, ~3 m, and ~2.2 m in Part 6 are interpreted as long-eccentricity, short-eccentricity, obliquity, and precession, respectively (Fig. 5a), and the inferred mean sedimentation rate was ~9 cm/kyr. These inferred rates in Parts 5 and 6 are broadly consistent with the paleomagnetically-derived sedimentation rates of Xiao et al. (2021) (~8.8 cm/kyr; Fig. 6). We note that some paleosols and carbonate nodules are developed in Parts 5 and 6, indicating a shallow water or subaerial exposure (e.g., Feng et al., 2010).

Inferred ~100 kyr short eccentricity cycles are a pervasive feature of the entire GZ-X501 section (Fig. 5). A floating astronomical time scale (ATS) can thus be constructed for the entire section by tuning each inferred short-eccentricity cycle to a fixed duration of 100 kyr. In total, there are ~109 short-eccentricity cycles in the PC1 data (Fig. 5). The same result is obtained for the K/Rb data (Supplementary Material Text 5, Fig. S5). We use PC1 for subsequent timescale construction (rather than K/Rb) as it captures the major paleoenvironmental variations since it is built from a matrix of multiple element proxies. Based on the ~109 short-eccentricity cycles, we obtain a ~10.9 Myr total duration for our section. This floating ATS is anchored to the base of the C27r polarity chron (~63.537 Ma in Gradstein et al., 2020, hereafter GTS2020) that Xiao et al. (2021) defined at the boundary of the Gonjo and Ranmugou

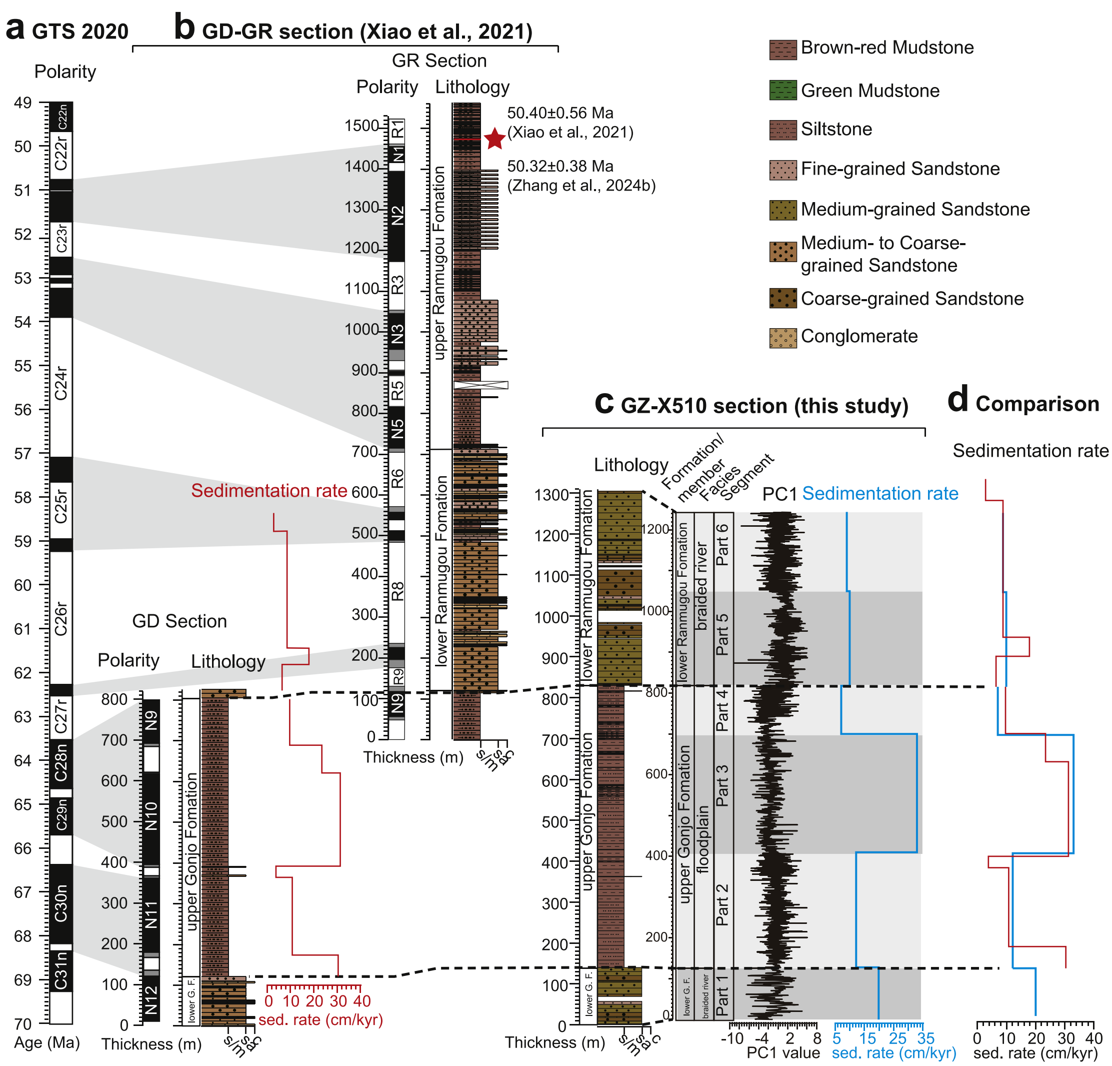

Fig. 6. Comparison of sedimentation rates estimated by magnetostratigraphy (from Xiao et al., 2021) and from COCO and spectral analysis (this study). (a) Geologic Time Scale (GTS2020; Gradstein et al., 2020). Sedimentation rate of GD-GR section (b) is estimated by the magnetostratigraphy inferred by Xiao et al. (2021). The magnetostratigraphy was calibrated to numerical time by Xiao et al. (2021) using a volcaniclastic zircon U-Pb date. This horizon (dated to 50.40 ± 0.56 Ma) is marked by a red star in b. An altered andesite zircon U-Pb date (50.32 ± 0.38 Ma, i.e. within error of Xiao et al.'s date) likely corresponds to the same horizon (Zhang et al., 2024b). Gray magnetozones highlight sampling gaps in the magnetostratigraphy. Sedimentation rate of GZ-X501 section (c) is interpreted by COCO analysis and spectral analysis (this study). (d) highlights the similarity of the sedimentation rate variations inferred for the GD-GR section and GZ-X501 sections (red line is average sedimentation rate in the GD-GR section, and blue lines is the sedimentation rate variations in the GZ-X501 section). Black dashed lines highlight lithostratigraphic correlation between GD-GR and GR-X501 sections.

formations (Fig. 1c-e). Thus, our ATS spans ~69.4 Ma to ~58.5 Ma, from the latest Cretaceous to early Paleocene (Fig. 7a-b).

The power spectrum of the 100 kyr-tuned PC1 data across the entire section shows significant (>99 % confidence level) peaks at periods of ~1238 kyr and ~178 kyr, close to the inferred periodicity of 1.2 Myr and ~173 kyr obliquity amplitude modulation (AM) cycles (Fig. 8a). In addition, ~405 kyr long-eccentricity and ~100 kyr short-eccentricity peaks (>99 % confidence level) occur (Fig. 8a). Peaks above 99 % confidence level also occur at ~53–46 kyr, ~38–35 kyr, ~29 kyr, ~27 kyr, ~25 kyr, ~23 kyr, and ~17 kyr, which coincide with expected obliquity and precession periods (Fig. 8a). Additional peaks at ~567 kyr and ~270–250 kyr may be unrelated to orbital forcing (Fig. 8a). These peaks, and at least some of the noise in our tuned record, could be due to the inability to fully account for short-term sedimentation rate changes and gaps in sedimentation/erosion in our record below the tuning scale used (100 kyr, short-eccentricity), and because tuning to a fixed duration of 100 kyr is in any case a simplification because short-eccentricity periods span 95–133 kyr in reality (Fig. 8b) (see also Section 5.1). As noted in Section 3.4, as a complementary approach the MTM power spectrum of the tuned PC1 data was calculated using the SWA method, with stringent 5 % FDR significance testing (Fig. S6). This analysis supports the veracity of our cyclostratigraphic interpretations and the tuned ATS, with strong evidence for eccentricity, obliquity and precession cycles (exceeding the 5 % FDR). Equally, the K/Rb data were also tuned to the same age model, and the power spectrum (and cycle significance) is consistent with the PC1 power spectrum (Fig. S6).

5. Discussion

5.1. A latest Cretaceous to early Paleocene timescale for the Gonjo Basin

Four correlation markers found in both the GZ-X501 and GD-GR sections serve as potential scrutinization points to test our ATS (Fig. 1c-e, Table 1). The first two markers are the lower and upper boundary of the upper Gonjo Formation, which, according to Xiao et al. (2021), correspond to the C30r/C31n (~140 m, 68.351 Ma in GTS2020) and C27r/C28n chron boundaries (830 m, 63.537 Ma in GTS2020). The third and fourth markers are two thick conglomerate layers (layer 1 at 977.4 m and layer 2 at 1129.75 m) in the lower Ranmugou formation. The conglomerate layer 1, according to Xiao et al. (2021), corresponds to C26r/C27n (62.278 Ma in GTS2020). Given the likely transience of the deposition of these conglomerate layers, the age of the conglomerate layer 2 is estimated using the average sedimentation rate of Xiao et al. (2021) after removal of the layers themselves, yielding an age of ~61

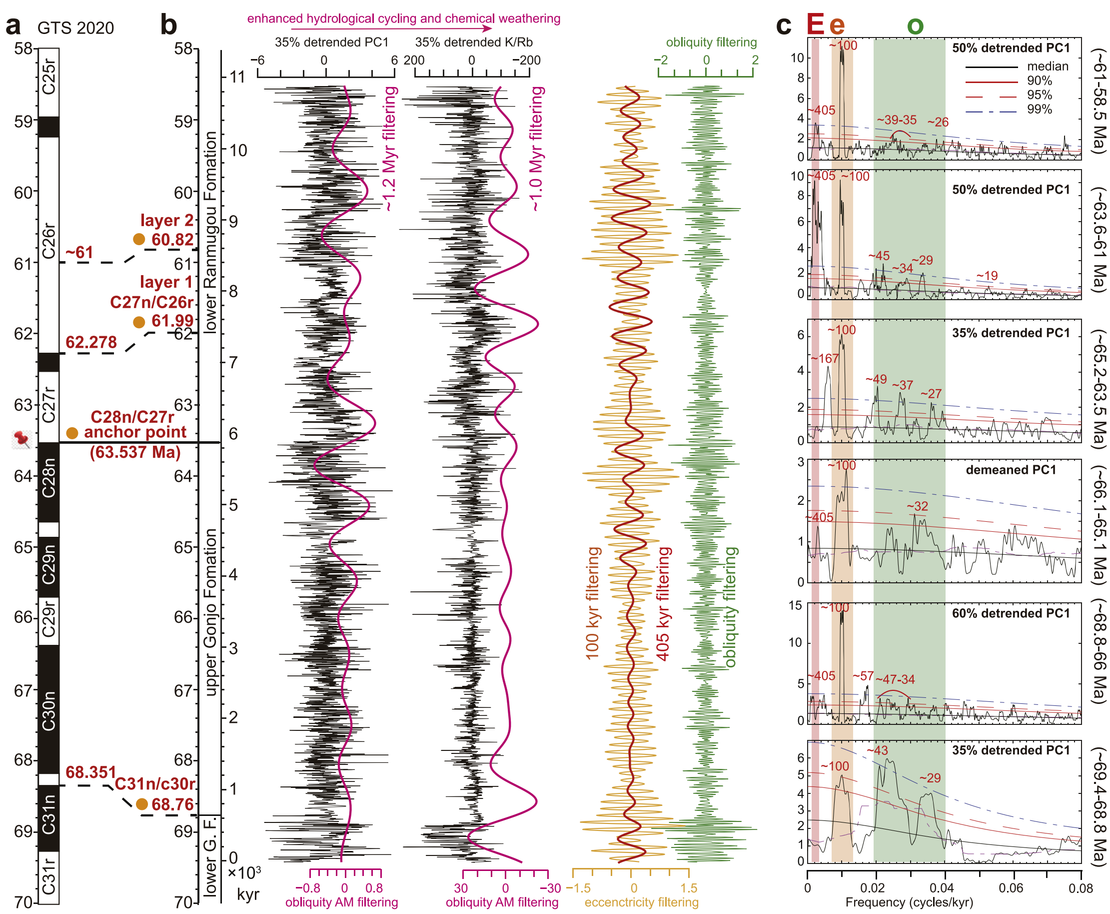

Fig. 7. Tuned PC1 and K/Rb data of the GZ-X501 section shown with orbital cycles and power spectra (2π MTM). (a) Geologic Time Scale (GTS2020; Gradstein et al., 2020), and filtered 405 kyr (red) and 100 kyr (orange) band of the La2010b solution (Laskar et al., 2011). (b) Tuned PC1 (left) and K/Rb (right) data (black lines, spanning ~69.4 Ma to ~58.5 Ma) with the astronomical time scale. Also shown are bandpass filter outputs of inferred ~1.2 Myr obliquity AM cycles (pink), 405 kyr (red) and 100 kyr (orange) eccentricity cycles of PC1 data, and inferred ~1.0 Myr obliquity AM cycles (pink), 405 kyr (red) and 100 kyr (orange) eccentricity cycles of K/Rb data. Four orange circles show the 4 key lithostratigraphic correlation layers as in Fig. 1. The thick black horizontal line shows the age of the anchor point used to fix the data in numerical time, based on the published age for the base of the C27r chron (63.537 Ma in GTS2020, Gradstein et al., 2020), as identified in the paleomagnetic record of Xiao et al. (2021). Three black dashed lines show comparison of our ATS and published ages of correlative horizons in the GD-GR composite section of Xiao et al. (2021) calibrated to GTS2020 (Gradstein et al., 2020) (see also Table 1). Gray shading and gray horizontal lines highlight the depositional environment transitions. (c) Power spectra (2π MTM) of the tuned PC1 data in each of the parts used for analysis of the untuned data (Fig. 5). Red, orange and green shading represents long-eccentricity, short-eccentricity and obliquity, respectively.

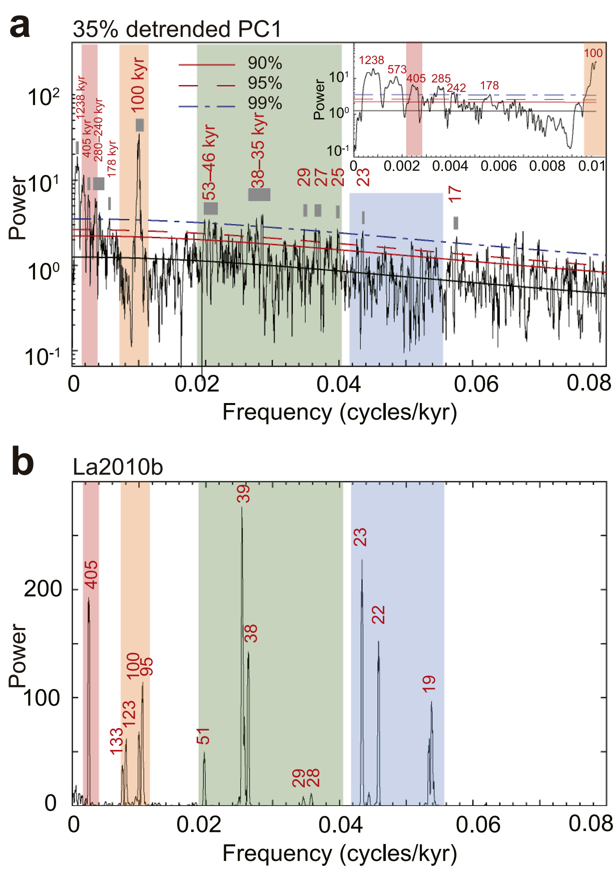

Fig. 8. Spectral analysis of the tuned PC1 data of the GZ-X501 section. (a) Power spectrum (2π MTM) of the tuned PC1 data (35 % rLOESS detrended) (inset figure shows detail at low frequencies). Tuning was based on the inferred 100 kyr short-eccentricity cycles (see also Fig. 5). (b) Power spectrum (2π MTM) of the ETP signal of La2010b solution (Laskar et al., 2011). Red, orange, green and blue shading represents long-eccentricity, short-eccentricity, obliquity, and precession, respectively.

Ma.

The C27r/C28n chron boundary serves as the anchor point for our ATS. Our ATS implies an age of 68.76 Ma for the C30r/C31n chron boundary, which is 0.41 Myr older than the age in Xiao et al. (2021) and GTS2020 (Fig. 7a-b and Table 1). Our ATS also implies ages of 61.99 and 60.82 Ma for conglomerate layers 1 and 2, which are 0.29 Myr and ~0.18 Myr younger than the ages estimated from the paleomagnetism of Xiao et al. (2021), respectively (Fig. 7a-b and Table 1). The inferred basal age for our section is 69.42 Ma, and this is broadly consistent with the basal age (~69 Ma) in Xiao et al. (2021) (Table 1). The top age cannot be compared with Xiao et al. (2021) as there is no clear lithological marker that allows the top of our GZ-X501 section to be correlated to Xiao et al.'s GD-GR section. The age of the scrutinization points of our ATS are generally quite close to the Xiao et al. (2021) reported ages, and differences do not exceed 0.42 Myr. This correspondence broadly supports the veracity of our ATS, and hence our new high-resolution timescale provides a robust temporal framework for the Gonjo Basin.

Age uncertainties in our ATS can arise in two ways: (1) uncertainties in the paleomagnetic interpretation of Xiao et al. (2021); and (2) uncertainties in our ATS. Regarding the first issue, we note that there is a sampling gap of 15 m in the paleomagnetic samples obtained by Xiao et al. (2021) between the C30r/C31n chron boundary and the succeeding sampling point (between 120 m and 135 m in the GD section) (indicated in gray on Fig. 1d). Sampling gaps of 4 m and 9 m also occur below and above the C27r/C28n chron boundary (120 m in the GR section), and gaps of 4 m and 6 m occur either side of the C26r/C27n chron boundary (228 m of GR section) (Fig. 1d). These sampling gaps create uncertainty in the precise chron boundary positions, though the errors they create are likely <0.14 Myr. A bigger issue would be if the paleomagnetic interpretation of Xiao et al. (2021) was incorrect. Indeed, there is only one absolute age that provides constraints on the palaeomagnetic interpretation. However, the veracity of their magnetostratigraphy is supported by the recent zircon U-Pb date obtained by Zhang et al. (2024b), likely from the same stratigraphic horizon dated by Xiao et al. (2021) that was used to anchor their timescale. These dates (50.40 Ma ± 0.56 Ma in Xiao et al., 2021 and 50.32 ± 0.38 Ma in Zhang et al., 2024b) are within error (Fig. 1d). The generally good correspondence between sedimentation rates inferred from the magnetostratigraphy in Xiao et al. (2021) and the sedimentation rates inferred from our cyclostratigraphy (which was built independently of the magnetostratigraphy) also supports the paleomagnetic age model (Fig. 6).

A possible source of error in our ATS is the use of 100 kyr short-eccentricity cycles to constrain the time scale. As noted in Section 4.2.2, short-eccentricity periods span 95–133 kyr in reality (Fig. 8b). Ideally, we would use the more stable 405 kyr long-eccentricity to tune and create our ATS. However, 405 kyr long-eccentricity cycles are weak in the Gonjo Formation, whereas 100 kyr short-eccentricity is a pervasive feature throughout the whole section (Fig. 5). Spectral analysis of the entire 100 kyr-tuned PC1 record does nevertheless shows a significant ~405 kyr cycle (Figs. 8a and S6c), supporting the robustness of our ATS since in general since it can be expected that orbital periods in a succession with unsteady sedimentation rate would be amplified when correctly tuned.

Given the complexity and variability of depositional processes of continental sediments, sedimentation rate changes and undetected gaps (such as those caused by erosion, conglomerate layers etc.) could affect our ATS, despite our tuning efforts. These irregular disturbances in the stratigraphy may lead to distortions of the orbital cycles. We note in particular that our measured thickness of the lower Gonjo Formation (~140 m) and the upper Gonjo Formation (~690 m) in the GZ-X501 section are slightly different to those of Xiao et al. (2021) (~120 m and ~680 m, respectively) (Fig. 1d-e, Supplementary Material Text 1). Thus, sedimentation rate changes between coeval outcrops (as well as field measurement errors), could constitute a minor source of error in our ATS. Related to this, a likely more important caveat to the veracity of our ATS is that in the predominantly fluvial depositional environment we have studied (with high lithological variability) stratigraphic

Table 1
A comparison of the GZ-X501 ATS in this study and published ages of correlative horizons in the GD-GR composite section of Xiao et al. (2021).

	This study (GZ-X501 section)		Xiao et al. (2021) (GD-GR section)			
Boundary	Depth (m)	ATS age (Ma)	Depth (m) (Fig. 1)	Published age (Ma)	Difference (Myr)	Reference
Base	0	69.42	GD-0	~69	~0.42	Xiao et al. (2021)
C30r/C31n	140.25	68.76	GD-120	68.351	0.41	GTS2020[1]
C27r/C28n	**830**	**63.537**	**GR-120**	**63.537**	**anchor**	**GTS2020**[1]
C26r/C27n	977.4	61.99	GR-228	62.278	−0.29	GTS2020[1]
Conglomerate layer 2	1129.75	60.82	GR-335	~61	~−0.18	Xiao et al. (2021)

[1] GTS2020 refers to Gradstein et al. (2020).

incompleteness caused by erosion and/or extended periods of non-deposition can be expected. This may cause errors in both our ATS and the magnetostratigraphy of Xiao et al. (2021). The general consistency of the durations inferred by our ATS and the magnetostratigraphy of Xiao et al. (2021) does, however, suggest that our record may indeed be stratigraphically complete at the 100 kyr scale.

5.2. Orbital scale hydroclimate variability in the Gonjo Basin during the latest Cretaceous to early Paleocene

The sedimentology of the GZ-X501 section and the geochemical data allows the paleoenvironmental evolution of the studied ~69.4 to ~58.5 Ma interval to be divided into three stages, matching the existing lithostratigraphic subdivisions (Fig. 7). Notably, two key transitions occurred, with a shift from braided river conditions to floodplain-dominated conditions at ~68.8 Ma, followed by a return to braided river conditions at ~63.5 Ma (Fig. 7). Previous studies indicate that the Gonjo Basin remained at a relatively low elevation (~0.7 km) until the early Eocene (~52 Ma) (Xiong et al., 2022; Ding et al., 2022), and that the sediment source in the basin was relatively stable, and mainly from Songpan-Ganzi Block and Northern Qiangtang Terrane (Bian, 2021). Anisotropy of magnetic susceptibility (AMS) results from central Gonjo Basin suggested an ENE-WSW post-depositional asymmetric compression (Xiao et al., 2021), or increased shortening strain after ~52 Ma (Li et al., 2020b). The analysis of paleocurrent and gravel components likely implies the changes of stream direction or position (Bian, 2021). As such, the tectonic setting and sediment source of the Gonjo Basin was likely relatively stable during the studied latest Cretaceous to early Paleocene interval, with the observed facies changes influenced primarily by climatic or autogenic evolution of the depositional system, rather than tectonism.

At the orbital scale, spectral analysis of the tuned PC1 data shows significant long- and short-eccentricity cycles (~405 kyr and ~100 kyr), as well as peaks at periods consistent with long and short obliquity cycles (~1.2 Myr, ~178 kyr and a cluster of peaks at periods of ~53–25 kyr) (Fig. 8). The ~1.2 Myr and ~178 kyr cycles could be related to the obliquity AM cycles of s4-s3 and s3-s6, respectively (e.g., Laskar et al., 2004; Laskar, 2020). Spectral analysis of tuned K/Rb is similar to the PC1 power spectrum (Fig. S6). PC1 is considered to reflect grain size changes, and K/Rb may reflect chemical weathering intensity (see Supplementary Material Text 3). Relatively humid conditions can result in high energy streamflow with increased grain size (higher PC1 values), and enhanced chemical weathering (lower K/Rb) (see Section 4.1 and Fig. 2). As such, the observed orbital-scale variations in PC1 and K/Rb strongly suggest eccentricity and obliquity forcing of hydrological conditions in the Gonjo Basin.

5.2.1. Eccentricity

Spectral analysis of the segmented PC1 data shows significant short-eccentricity across the whole section, and a long-eccentricity signal within the 63.6–58.5 Ma interval (Part 5–6, ~818–1244.25 m, lower Ranmugou Formation, braided river environment) (Figs. 5 and 7). The short duration of the Part 1 and Part 3–4 intervals (<2 Ma) likely compromises the ability to identify 405 kyr long eccentricity cycles in these parts. In detail, the short- and long- eccentricity filter curves of the PC1 data in Fig. 7b show higher amplitudes at ~65–58.5 Ma (mostly within the lower Ranmugou Formation, braided river environment) compared to ~69.4–65 Ma (mostly within the upper Gonjo Formation, floodplain environment). Thus, eccentricity strength is likely dependent at least in part to the depositional environment.

The lower Gonjo Formation (~69.4–68.8 Ma) and upper Ranmugou formation (~63.5–58.5 Ma) are characterized by braided river deposits, and high K/Rb values in this interval (Fig. 7b) suggest relatively low chemical weathering and a relatively arid climate. By contrast, the upper Gonjo Formation (~68.8–63.5 Ma) is characterized by floodplain deposits, and generally low K/Rb values (Fig. 7b) suggest relatively higher chemical weathering and more humid conditions. Thus, the relatively strong eccentricity signal in PC1 in the lower Ranmugou Formation may have been related to the more variable braided river depositional environment, perhaps with periodically intense rainfall and/or regular avulsion (given the stronger seasonality implied by stronger eccentricity). By contrast, the weaker eccentricity signal in the upper Gonjo Formation may be a consequence of the more quiescent and stable floodplain environment. However, eccentricity amplitude variations in K/Rb differ from the PC1 eccentricity variations (Fig. 7b). The amplitude of the eccentricity cycle in K/Rb is relatively stable, with a slightly weaker amplitude during ~68.5–67 Ma (Fig. 7b). Together, these data suggest differential responses to eccentricity forcing in different proxies, as has been previously demonstrated by Li et al. (2019a).

Many Late Cretaceous-Paleogene paleoclimate records from East Asia and globally show a clear eccentricity signal. For example, Zhang et al. (2024b) reported eccentricity (found in Fe/Mn and Ti/Ca variations) forcing of the water level in the Gonjo Basin across the Early Eocene Climatic Optimum. In the oceans, dominant eccentricity signals have been found in lightness (L*, reflecting relative abundance of carbonate versus clay), MS and lithological log records from Zumaia and Sopelana in the Basque-Cantabric Basin in the late Maastrichtian (Batenburg et al., 2012, 2014). Eccentricity is also recognized in benthic foraminifera carbon and oxygen isotopes ($\delta^{13}C_b$ and $\delta^{18}O_b$) and sediment coarse fraction data from ODP Site 1262 through the Late Cretaceous to early Eocene (Littler et al., 2014; Barnet et al., 2019). These data suggest eccentricity was a strong pacemaker of Late Cretaceous-Paleogene climate change and carbon cycling. On their own, eccentricity variations are insufficient to modulate climate changes directly (as eccentricity has little effect on insolation), however, eccentricity modulates the amplitude of precession and can hence control low latitude seasonality by changing the strength and length of seasons (Ruddiman, 2008). As such, the strong eccentricity control on the hydroclimate of the Gonjo Basin that we observe can potentially be explained via a control on intra-annual variations in precipitation and temperature. Precession itself is relatively weak in our data owing to the low sampling resolution relative to the duration of precession cycles, which makes these cycles harder to resolve via spectral analysis (e.g., Kemp, 2016).

5.2.2. Obliquity

The influence of obliquity at low latitudes, especially during relatively warm and largely ice-free intervals of Earth history such as the latest Cretaceous to early Paleocene, is negligible because obliquity has little effect on low-latitude insolation changes/seasonality (Raymo et al., 2006). Nevertheless, obliquity signals have been detected in other greenhouse climate records at relatively low latitudes. For example, ~41 kyr obliquity cycles were detected in benthic foraminifera $\delta^{13}C_b$, $\delta^{18}O_b$ from ODP Site 1262 (south Atlantic Ocean) during the late Maastrichtian to early Paleocene (Barnet et al., 2019). Significant obliquity cycles were also found in Fe data from ODP Site 1258 (tropical western Atlantic) in the middle of magnetochron C22r (~50.1–49.4 Ma; Westerhold and Rohl, 2009). Putative obliquity cycles (~50–30 kyr periods) were detected in MS data from the middle to late Eocene in the Weihe Basin, which suggests that obliquity paced hydroclimate change in this basin (Zhang et al., 2023). Obliquity AM cycles (~1.3 Myr) were also found in MS, GR and marine biodiversity data from the late early Permian, South China (Fang et al., 2023). Similarly, ~1.2 Myr obliquity AM cycles have also been found in Early Triassic South China (Li et al., 2016).

To assess the temporal pattern of obliquity strength in our data, the ratio between obliquity power and total power in the data was measured via a sliding window analysis (denoted as O/T; Fig. 9). We compared this to the obliquity strength measured in the same way in benthic foraminifera $\delta^{13}C_b$ and $\delta^{18}O_b$ data from ODP Site 1262 (Westerhold et al., 2020). ODP Site 1262 preserves a high-resolution marine record with a precise ATS, and covers most of our studied interval in the Gonjo Basin,

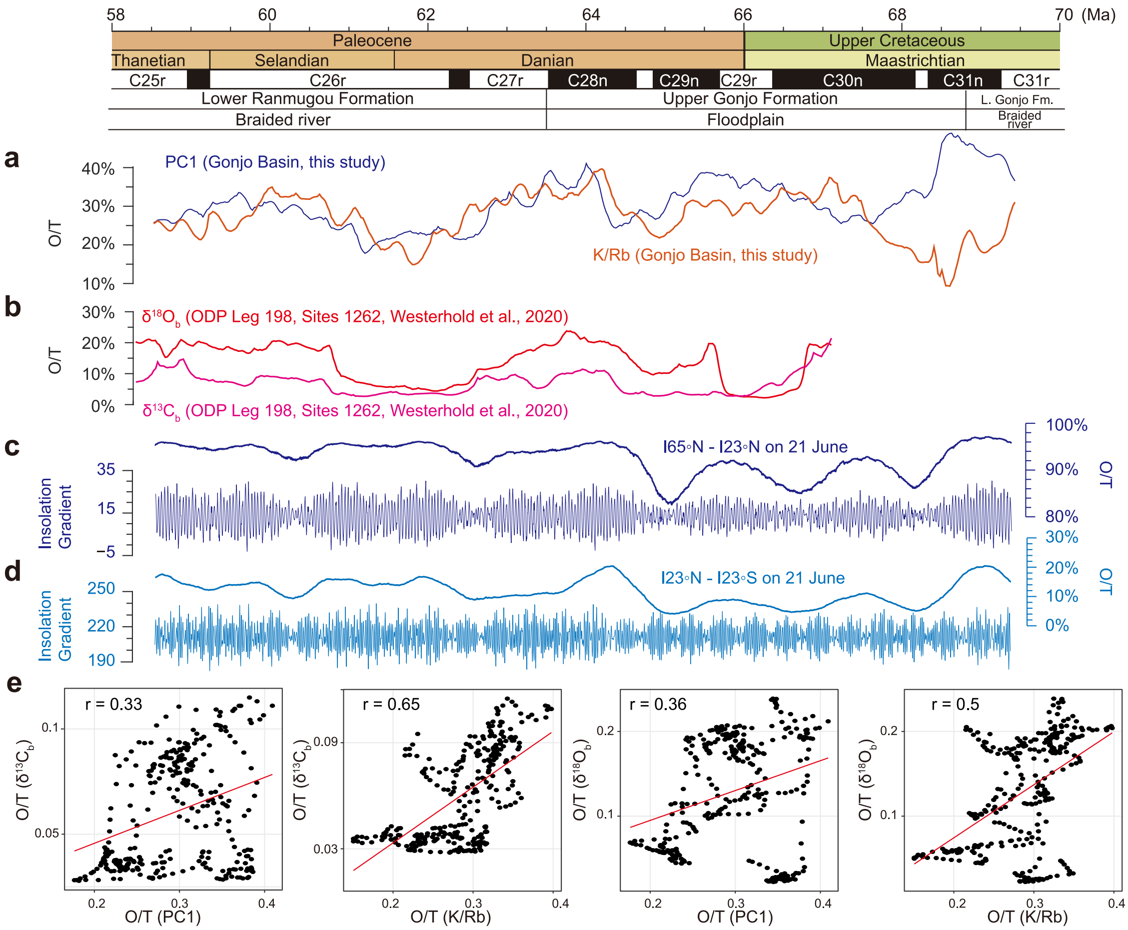

Fig. 9. Obliquity power changes during latest Cretaceous to early Paleocene. (a) Observed O/T (obliquity variance/total variance) of PC1 (blue) and K/Rb (orange) series in time domain. (b) Observed O/T (obliquity variance/total variance) of benthic foraminifera $\delta^{13}C_b$, $\delta^{18}O_b$ from ODP Sites 1262 (Westerhold et al., 2020) (c) Equator-to-pole insolation gradient (Insolation 65°N–Insolation 23°N on 21st June) of La2010b insolation solution (Laskar et al., 2011), and its observed O/T. (d) Inter-tropical insolation gradient (Insolation 23°N–Insolation 23°S on 21st June) of La2010b (Laskar et al., 2011), and its observed O/T. O/T were calculated via a 1000 kyr sliding window with 5 kyr step. (e) Scatter plots and Pearson correlation coefficient values showing the relationships between observed O/T of PC1, K/Rb, $\delta^{13}C_b$, and $\delta^{18}O_b$ during ~59–66.6 Ma. Note that p-values are not calculated for these correlations as O/T values are not independent of each other.

making it the most suitable site to investigate any similarities or differences in the orbital forcing response of terrestrial versus marine data. There are similarities between obliquity strength variations in our PC1 and K/Rb data with those in the $\delta^{13}C_b$ and $\delta^{18}O_b$ data (Fig. 9a-b). Specifically, intervals of high relative obliquity power (higher O/T) in our PC1 data (between ~59 and 61 Ma, and ~62.5 and 64.5 Ma) are coeval with similarly high O/T in $\delta^{13}C_b$ and $\delta^{18}O_b$ (Fig. 9a-b). Pronounced minima in O/T in our PC1 and K/Rb data between ~61 and 62.5 Ma are also matched by minima in the O/T of the $\delta^{13}C_b$ and $\delta^{18}O_b$ (Fig. 9a-b).

Correlation analysis supports a moderate positive correlation between Gonjo Basin obliquity strength and ODP Site 1262 obliquity strength (Fig. 9e). Overall, this suggests that our terrestrial data are reflecting changes in obliquity strength consistent with globally representative data from the oceans. However, the match between these empirical data and calculated theoretical O/T over the studied interval (Laskar et al., 2011) is less clear (Fig. 9a-d). Notably, a rise in calculated O/T at ~64.5 Ma is not observed in either our data or the marine data (Fig. 9a-d).

Interestingly, the overall relative strength of obliquity is higher in the Gonjo Basin than in the marine data (Fig. 9a-b and e), suggesting an increased sensitivity to obliquity on the east Asian continent relative to the oceans. This may be due to the lower heat capacity of the land compared to the oceans, so temperatures on land are more variable and hydrological variations may be stronger. Our work is consistent with previous studies (e.g., Westerhold and Röhl, 2009; Li et al., 2016; Fang et al., 2023; Zhang et al., 2023) that show how obliquity can play an important role in controlling greenhouse climate variability, and thus may have helped to pace regional hydrological changes in the Gonjo Basin.

The obliquity cycles found in climate records from low latitudes may be remotely controlled by high-latitude climate cyclicity (Westerhold and Röhl, 2009). The possible existence of ephemeral ice sheets at high latitudes during the latest Cretaceous (e.g., Huber et al., 2018) may have amplified the role of obliquity as a driver of climate change. However, in the absence of amplifying effects from large ice sheets, high latitude obliquity signals may have been transported to low latitudes via atmospheric and ocean circulation processes (Westerhold and Röhl, 2009). Obliquity controls the equator-to-pole meridional insolation gradients, and thus the poleward transport of heat, moisture and latent energy (Raymo and Nisancioglu, 2003; Zhang et al., 2024c). As such, during obliquity maxima the equator to pole insolation and temperature gradient would decrease and lead to a decrease in the poleward transport of heat and moisture (and vice versa during obliquity minima) (Raymo and Nisancioglu, 2003). Thus, high obliquity is associated with less moisture transport from the low latitudes to high-latitudes, and may lead to relatively enhanced hydrological cycling (yielding coarser grain-sizes and higher PC1 values) and stronger chemical weathering (low K/Rb) in the low-latitude Gonjo Basin (Fig. 7b). A similar mechanism has been invoked in deep-time greenhouse climates influenced by ~1.2 Myr obliquity AM cycles; with 1.2 Myr minima linked to reduced poleward transportation of heat and moisture, and vice versa (Li et al., 2016).

The mid-latitude Westerlies and tropical Easterlies, which may influence the transportation of water vapor to the Gonjo Basin, may be associated with obliquity forced meridional insolation gradients and surface pressure gradients (Lee and Poulsen, 2005). Lower obliquity, increased meridional insolation gradient and surface air temperature gradients may lead to intensified midlatitude Westerlies, subtropical trade winds, and subtropical gyre circulation (Lee and Poulsen, 2005), thus probably causing enhanced precipitation (i.e. coarser grain-size and higher PC1) and chemical weathering (related to low K/Rb) in the Gonjo Basin (Fig. 7b). Bosmans et al. (2015) suggested that obliquity can affect low latitude climate by modulating the cross-equatorial insolation gradient and tropical circulation changes. High obliquity can cause a high inter-tropical summer insolation gradient, and lead to an enhanced cross-equatorial moisture transport into the summer hemisphere (Bosmans et al., 2015), this may have caused stronger hydrological cycling and chemical weathering in the Gonjo Basin (Fig. 7b).

As a final point to note, the pattern of O/T changes of our data are similar to those in the oceanic $\delta^{13}C_b$ data (Fig. 9), which perhaps implies a connection between obliquity-forced global carbon cycle changes and hydrological cycling in the Gonjo Basin. Quasi-stable carbon reservoirs at middle to high latitudes may respond to the high latitude insolation and/or meridional insolation gradients (Huybers, 2006; Laurin et al., 2015; Huang et al., 2021). The mediation of quasi-stable carbon reservoirs could mediate global climate (e.g., DeConto et al., 2012; Ruppel and Kessler, 2017) and thus hydrological cycling, including the hydrology of the Gonjo Basin.

6. Conclusions

We conducted sedimentological, geochemical, and cyclostratigraphic analysis on an extremely thick succession of latest Cretaceous to early Paleocene strata in the Gonjo Basin (Southeast Tibet). Our work establishes a very long (>10 Myr) high-resolution astronomical timescale for the section, whilst also yielding a high-resolution record of paleoenvironment evolution (spanning ~69.4 Ma to ~58.5 Ma). The basin as a whole experienced a transition from a braided river to a floodplain environment, and back to braided river environment with strong seasonality during this time interval. Our cyclostratigraphic results indicate that the Gonjo Basin hydrological cycle at this time was influenced by the combination of eccentricity and obliquity, irrespective of local topographic changes. Eccentricity likely controlled seasonality and hydroclimate in the Gonjo Basin through its modulation of precession. The presence of obliquity forcing in the Gonjo Basin is less expected, and suggests a teleconnection between obliquity insolation variability at higher latitudes with hydrological cycling in the low latitude Gonjo Basin – most likely via changes in atmospheric circulation and/or carbon cycle modulation processes.

CRediT authorship contribution statement

Xiaoyue Zhang: Writing – original draft, Methodology, Investigation, Formal analysis, Data curation, Conceptualization. **David B. Kemp:** Writing – review & editing, Supervision, Funding acquisition, Formal analysis, Conceptualization. **Ruiyao Zhang:** Writing – review & editing, Formal analysis. **Robert A. Spicer:** Writing – review & editing. **Simin Jin:** Writing – review & editing. **Rui Zhang:** Writing – review & editing. **Ze Zhang:** Writing – review & editing, Formal analysis. **Chunju Huang:** Writing – review & editing, Supervision, Funding acquisition.

Declaration of competing interest

The authors declare that they have no known competing financial interests or personal relationships that could have appeared to influence the work reported in this paper.

Acknowledgements

We are grateful to Mengyang Hou for his assistance with field sampling. The work was supported by the National Natural Science Foundation of China (Grant No 42230208, 42272033, 42488201, 42172039), the China Postdoctoral Science Foundation (Grant No 2024M763058), the Postdoctoral Fellowship Program of CPSF (Grant No GZC20232476).

Supplementary materials

Supplementary material associated with this article can be found, in the online version, at doi:10.1016/j.epsl.2025.119306.

Data availability

Data will be made available on request.

References

Barnet, J.S.K., Littler, K., Westerhold, T., Kroon, D., Leng, M.J., Bailey, I., Röhl, U., Zachos, J.C., 2019. A high-fidelity benthic stable isotope record of late cretaceous–Early eocene climate change and carbon-cycling. Paleoceanogr. Paleocl. 34 (4), 672–691. https://doi.org/10.1029/2019PA003556.

Batenburg, S.J., Gale, A.S., Sprovieri, M., Hilgen, F.J., Thibault, N., Boussaha, M., Orue-Etxebarria, X., 2014. An astronomical time scale for the Maastrichtian based on the Zumaia and Sopelana sections (Basque Country, Northern Spain). JGS 171 (2), 165–180. https://doi.org/10.1144/jgs2013-015.

Batenburg, S.J., Sprovieri, M., Gale, A.S., Hilgen, F.J., Hüsing, S., Laskar, J., Liebrand, D., Lirer, F., Orue-Etxebarria, X., Pelosi, N., Smit, J., 2012. Cyclostratigraphy and astronomical tuning of the late Maastrichtian at Zumaia (Basque Country, Northern Spain). Earth Planet. Sci. Lett. 359–360, 264–278. https://doi.org/10.1016/j.epsl.2012.09.054.

BGMR Xizang, 1993. Regional Geology of Xizang (Tibet) Autonomous Region. Geological Memoirs Series. Geological House, Beijing.

Bian, Z., 2021. Master Thesis. Yunnan University.

Bosmans, J.H.C., Hilgen, F.J., Tuenter, E., Lourens, L.J., 2015. Obliquity forcing of low-latitude climate. Climate Past 11 (10), 1335–1346. https://doi.org/10.5194/cp-11-1335-2015.

DeConto, R.M., Galeotti, S., Pagani, M., Tracy, D., Schaefer, K., Zhang, T., Pollard, D., Beerling, D.J., 2012. Past extreme warming events linked to massive carbon release from thawing permafrost. Nature 484, 87–92. https://doi.org/10.1038/nature10929.

Ding, L., Kapp, P., Cai, F., Garzione, C.N., Xiong, Z., Wang, H., Wang, C., 2022. Timing and mechanisms of Tibetan Plateau uplift. Nat. Rev. Earth Env. 3, 652–667. https://doi.org/10.1038/s43017-022-00318-4.

Fang, Q., Wu, H., Shen, S., Fan, J., Hinnov, L., Yuan, D., Ren, C., Zhou, M., Zhang, S., Yang, T., Zhang, Y., Chen, J., Wu, Q., Liu, M., 2023. Long-period astronomical forcing of climatic and biological evolution during the late paleozoic icehouse-to-greenhouse transition. Earth. Sci. Rev. https://doi.org/10.1016/j.earscirev.2023.104402 null, null.

Feng, Z.Q., Jia, C.Z., Xie, X.N., Zhang, S., Feng, Z.H., Timothy, A.C., 2010. Tectonostratigraphic units and stratigraphic sequences of the nonmarine Songliao basin, northeast China. Basin Res. 22, 79–95.

Gao, Y., Ibarra, D.E., Caves Rugenstein, J.K., Chen, J., Kukla, T., Methner, K., Gao, Y., Huang, H., Lin, Z., Zhang, L., Xi, D., Wu, H., Carroll, A.R., Graham, S.A., Chamberlain, C.P., Wang, C., 2021. Terrestrial climate in Mid-latitude East Asia from the latest cretaceous to the earliest paleogene: a multiproxy record from the Songliao Basin in northeastern China. Earth-Sci. Rev. 216, 103572. https://doi.org/10.1016/j.earscirev.2021.103572.

Gradstein, F.M., Ogg, J.G., Schmitz, M.D., Ogg, G.M. (Eds.), 2020. Geologic Time Scale 2020. Elsevier.

He, S.Y., Tian, Y.H., Chen, K.G., Chen, Q.Y., Wen, H.C., 1983. Paleogene Gonjo red beds in East Tibet. Contributions to Tibetan Geology. Editor T. D. Li. Geological Publish House, Beijing, pp. 233–242 in Chinese with English abstract.

Huang, H., Gao, Y., Ma, C., Jones, M.M., Zeeden, C., Ibarra, D.E., Wu, H., Wang, C., 2021. Organic carbon burial is paced by a ~173-ka obliquity cycle in the middle to high latitudes. Sci. Adv. 7 (28), eabf9489. https://doi.org/10.1126/sciadv.abf9489.

Huber, B.T., MacLeod, K.G., Watkins, D.K., Coffin, M.F., 2018. The rise and fall of the cretaceous Hot Greenhouse climate. Glob. Planet Change 167, 1–23. https://doi.org/10.1016/j.gloplacha.2018.04.004.

Huybers, P., 2006. Early pleistocene glacial cycles and the integrated summer insolation forcing. Science (1979) 313, 508–511. https://doi.org/10.1126/science.1125249.

IPCC, 2023. Sections. In: Climate Change 2023: Synthesis Report. Contribution of Working Groups I, II and III to the Sixth Assessment Report of the Intergovernmental Panel on Climate Change [Core Writing Team, H. Lee and J. Romero (eds.)]. Geneva, Switzerland. IPCC, pp. 35–115. https://doi.org/10.59327/IPCC/AR6-9789291691647.

Jolliffe, I.T., Cadima, J., 2016. Principal component analysis: a review and recent developments. Philos. Trans. A Math. Phys. Eng. Sci. 374 (2065), 20150202. https://doi.org/10.1098/rsta.2015.0202.

Kemp, D.B., 2016. Optimizing significance testing of astronomical forcing in cyclostratigraphy. Paleoceanography 31 (12), 1516–1531. https://doi.org/10.1002/2016pa002963.

Kodama, K.P., Hinnov, L.A., 2014. Rock Magnetic cyclostratigraphy, Rock magnetic cyclostratigraphy. https://doi.org/10.1002/9781118561294.

Lanci, L., Galeotti, S., Ratcliffe, K., Tohver, E., Wilson, A., Flint, S., 2022. Astronomically forced cycles in middle permian fluvial sediments from Karoo Basin (South Africa). Palaeogeogr. Palaeoclimatol. Palaeoecol. 596, 110973. https://doi.org/10.1016/j.palaeo.2022.110973.

Laskar, J., 2020. Astrochronology. Geologic Time Scale 2020. Elsevier, pp. 139–158. https://doi.org/10.1016/B978-0-12-824360-2.00004-8.

Laskar, J., Fienga, A., Gastineau, M., Manche, H., 2011. La2010: a new orbital solution for the long term motion of the Earth. Physics (College Park. Md). https://doi.org/10.1051/0004-6361/201116836.

Laskar, J., Robutel, P., Joutel, F., Gastineau, M., Correia, A.C.M., Levrard, B., 2004. A long-term numerical solution for the insolation quantities of the Earth. Astron. Astrophys. 428 (1), 261–285. https://doi.org/10.1051/0004-6361:20041335.

Laurin, J., Meyers, S.R., Uličný, D., Jarvis, I., Sageman, B.B., 2015. Axial obliquity control on the greenhouse carbon budget through middle- to high-latitude reservoirs. Paleoceanography 30 (2), 133–149. https://doi.org/10.1002/2014PA002736.

Lee, S.Y., Poulsen, C.J., 2005. Tropical Pacific climate response to obliquity forcing in the pleistocene. Paleoceanography 20 (4), 2005PA001161. https://doi.org/10.1029/2005PA001161.

Li, M., Huang, C., Ogg, J., Zhang, Y., Hinnov, L., Wu, H., Chen, Z.-Q., Zou, Z., 2019a. Paleoclimate proxies for cyclostratigraphy: comparative analysis using a lower triassic marine section in South China. Earth-Sci. Rev. 189, 125–146. https://doi.org/10.1016/j.earscirev.2019.01.011.

Li, M., Hinnov, L., Kump, L., 2019b. Acycle: time-series analysis software for paleoclimate research and education. Comput. Geosci. 127, 12–22. https://doi.org/10.1016/j.cageo.2019.02.011.

Li, M., Kump, L.R., Hinnov, L.A., Mann, M.E., 2018. Tracking variable sedimentation rates and astronomical forcing in phanerozoic paleoclimate proxy series with evolutionary correlation coefficients and hypothesis testing. Earth Planet. Sci. Lett. 501, 165–179. https://doi.org/10.1016/j.epsl.2018.08.041.

Li, M., Huang, C., Hinnov, L., Ogg, J., Chen, Z.-Q., Zhang, Y., 2016. Obliquity-forced climate during the early triassic hothouse in China. Geology 44 (8), 623–626. https://doi.org/10.1130/G37970.1.

Li, S., van Hinsbergen, D.J.J., Najman, Y., Liu-Zeng, J., Deng, C., Zhu, R., 2020a. Does pulsed Tibetan deformation correlate with Indian plate motion changes? Earth Planet. Sci. Lett. 536, 116144. https://doi.org/10.1016/j.epsl.2020.116144.

Li, S., van Hinsbergen, D.J.J., Shen, Z., Najman, Y., Deng, C., Zhu, R., 2020b. Anisotropy of magnetic susceptibility (AMS) analysis of the Gonjo Basin as an independent constraint to date Tibetan shortening pulses. Geophys. Res. Lett. 47, e2020GL087531. https://doi.org/10.1029/2020GL087531.

Littler, K., Röhl, U., Westerhold, T., Zachos, J.C., 2014. A high-resolution benthic stable-isotope record for the South Atlantic: implications for orbital-scale changes in late paleocene–Early eocene climate and carbon cycling. Earth Planet. Sci. Lett. 401, 18–30. https://doi.org/10.1016/j.epsl.2014.05.054.

Ma, M., Zhang, W., Zhao, M., Qiu, Y., Cai, H., Chen, J., Liu, X., 2022. Deccan traps volcanism implicated in the extinction of Non-Avian dinosaurs in southeastern China. Geophys. Res. Lett. 49 (24). https://doi.org/10.1029/2022GL100342.

Ma, M., He, M., Zhao, M., Peng, C., Liu, X., 2021. Evolution of atmospheric circulation across the cretaceous–Paleogene (K–Pg) boundary interval in low-latitude East Asia. Global Planet Change 199, 103435. https://doi.org/10.1016/j.gloplacha.2021.103435.

Ma, M., Liu, X., Wang, W., 2018. Palaeoclimate evolution across the cretaceous–Palaeogene boundary in the Nanxiong Basin (SE China) recorded by red strata and its correlation with marine records. Clim. Past 14 (3), 287–302. https://doi.org/10.5194/cp-14-287-2018.

Mann, M.E., Lees, J.M., 1996. Robust estimation of background noise and signal detection in climatic time series. Clim. Chang. 33, 409–445. https://doi.org/10.1007/BF00142586.

Raymo, M.E., Lisiecki, L.E., Nisancioglu, K.H., 2006. Plio-Pleistocene Ice volume, antarctic climate, and the global δ18O record. Sci., New Series 313 (5786), 492–495.

Raymo, M.E., Nisancioglu, K.H., 2003. The 41 kyr World: milankovitch's other unsolved mystery. Paleoceanography 18 (1), 2002PA000791. https://doi.org/10.1029/2002PA000791.

Ruddiman, W.F., 2008. Earth's Climate: Past and Future, 2nd ed. W. H, Freeman and Company.

Ruppel, C.D., Kessler, J.D., 2017. The interaction of climate change andmethane hydrates. Rev. Geophys. 55, 126–168. https://doi.org/10.1002/2016RG000534.

Spurlin, M.S., Yin, A., Horton, B.K., Zhou, J., Wang, J., 2005. Structural evolution of the Yushu-Nangqian region and its relationship to syncollisional igneous activity, east-central Tibet. Geol. Soc. Am. Bull. 117, 1293–1317.

Studnicki-Gizbert, C., Burchfiel, B.C., Li, Z., Chen, Z., 2008. Early tertiary Gonjo Basin, Eastern Tibet: sedimentary and structural record of the Early history of India-Asia collision. Geosphere 4 (4), 713. https://doi.org/10.1130/GES00136.1.

Sun, X., Wang, P., 2005. How old is the Asian monsoon system?—Palaeobotanical records from China. Palaeogeogr. Palaeoclimatol. Palaeoecol. 222 (3–4), 181–222. https://doi.org/10.1016/j.palaeo.2005.03.005.

Tang, M., Liu-Zeng, J., Hoke, G.D., Xu, Q., Wang, W., Li, Z., Zhang, J., Wang, W., 2017. Paleoelevation reconstruction of the Paleocene-Eocene Gonjo Basin, SE-Central Tibet. Tectonophysics 712–713, 170–181. https://doi.org/10.1016/j.tecto.2017.05.018.

Thomson, D.J., 1982. Spectrum estimation and harmonic analysis. Proc. IEEE 70, 1055–1096. https://doi.org/10.1109/PROC.1982.12433.

Wang, C., Scott, R.W., Wan, X., Graham, S.A., Huang, Y., Wang, P., Wu, H., Dean, W.E., Zhang, L., 2013. Late cretaceous climate changes recorded in Eastern Asian lacustrine deposits and North American epieric Sea strata. Earth-Sci. Rev. 126, 275–299. https://doi.org/10.1016/j.earscirev.2013.08.016.

Weedon, G.P., Page, K.N., Jenkyns, H.C., 2019. Cyclostratigraphy, stratigraphic gaps and the duration of the Hettangian Stage (Jurassic): insights from the Blue Lias formation of Southern Britain. Geol. Mag. 156, 1469–1509. https://doi.org/10.1017/S0016756818000808.

Westerhold, T., Marwan, N., Drury, A.J., Liebrand, D., Agnini, C., Anagnostou, E., Barnet, J.S.K., Bohaty, S.M., De Vleeschouwer, D., Florindo, F., Frederichs, T., Hodell, D.A., Holbourn, A.E., Kroon, D., Lauretano, V., Littler, K., Lourens, L.J., Lyle, M., Pälike, H., Röhl, U., Tian, J., Wilkens, R.H., Wilson, P.A., Zachos, J.C., 2020. An astronomically dated record of Earth's climate and its predictability over the last 66 million years. Science (1979) 369 (6509), 1383–1387. https://doi.org/10.1126/science.aba6853.

Westerhold, T., Röhl, U., 2009. High resolution cyclostratigraphy of the early eocene – New insights into the origin of the cenozoic cooling trend. Clim. Past.

Wu, H., Zhang, S., Hinnov, L.A., Jiang, G., Yang, T., Li, H., Wan, X., Wang, C., 2014. Cyclostratigraphy and orbital tuning of the terrestrial upper Santonian–Lower Danian in Songliao Basin, northeastern China. Earth Planet. Sci. Lett. 407, 82–95. https://doi.org/10.1016/j.epsl.2014.09.038.

Wu, H., Zhang, S., Jiang, G., Hinnov, L., Yang, T., Li, H., Wan, X., Wang, C., 2013. Astrochronology of the early turonian–Early campanian terrestrial succession in the Songliao Basin, northeastern China and its implication for long-period behavior of the Solar system. Palaeogeogr. Palaeocl. 385, 55–70. https://doi.org/10.1016/j.palaeo.2012.09.004.

Wu, H., Zhang, S., Jiang, G., Huang, Q., 2009. The floating astronomical time scale for the terrestrial late cretaceous Qingshankou Formation from the Songliao Basin of Northeast China and its stratigraphic and paleoclimate implications. Earth Planet. Sci. Lett. 278 (3–4), 308–323. https://doi.org/10.1016/j.epsl.2008.12.016.

Xiao, R., Zheng, Y., Liu, X., Yang, Q., Liu, G., Xia, L., Bian, Z., Guan, J., Feng, P., Xu, H., Clift, P.D., Qiang, X., Zhang, Y., Zheng, H., 2021. Synchronous sedimentation in Gonjo Basin, Southeast Tibet in response to India-Asia collision constrained by magnetostratigraphy. Geochem. Geophy. Geosy. 22 (3). https://doi.org/10.1029/2020GC009411.

Xiong, Z., Ding, L., Spicer, R.A., Farnsworth, A., Wang, X., Valdes, P.J., Su, T., Zhang, Q., Zhang, L., Cai, F., Wang, H., Li, Z., Song, P., Guo, X., Yue, Y., 2020. The early eocene rise of the Gonjo Basin, SE Tibet: from low desert to high forest. Earth Planet. Sci. Lett. 543, 116312. https://doi.org/10.1016/j.epsl.2020.116312.

Xiong, Z., Liu, X., Ding, L., Farnsworth, A., Spicer, R.A., Xu, Q., Valdes, P., He, S., Zeng, D., Wang, C., Li, Z., Guo, X., Su, T., Zhao, C., Wang, H., Yue, Y., 2022. The rise and demise of the paleogene Central Tibetan Valley. Sci. Adv. 8, eabj0944. https://doi.org/10.1126/sciadv.abj0944.

Zachos, J., Pagani, M., Sloan, L., Thomas, E., Billups, K., 2001. Trends, rhythms, and aberrations in global climate 65 ma to present. Science (1979) 292 (5517), 686–693. https://doi.org/10.1126/science.1059412.

Zhang, R., Huang, C., Kemp, D.B., Wang, Z., Zhang, Z., Chen, W., 2023. Astronomical forcing of the hydrological cycle in the Weihe Basin (North China) during the middle to late eocene. Glob. Planet. Change 228, 104208. https://doi.org/10.1016/j.gloplacha.2023.104208.

Zhang, Z., Zhang, Z., Zhang, Z., Tan, N., He, Z., Huang, C., Guo, Z., 2024a. Resolving cenozoic climate pattern debate in East Asia: insights from orbital-scale oscillations. Glob. Planet. Change 232, 104346.

Zhang, R., Huang, C., Kemp, D.B., Zhang, Z., Wang, Z., Zhang, X., Zhao, D., Jin, S., Zhang, R., 2024b. Eccentricity forcing of the hydrological cycle in East Asia during the early eocene climatic optimum (EECO). JGR Atmospheres 129 (2), e2023JD040314. https://doi.org/10.1029/2023JD040314.

Zhang, Z., Rohling, E.J., Kemp, D.B., Wang, Z., Huang, C., 2024c. Orbital scale global ocean sea surface temperatures coupling with cryospherecarbon cycle changes over the past 4 million years. Paleoceanogr. Paleoclimatol. 39, e2024PA004856. https://doi.org/10.1029/2024PA004856.